Escola de Camins
Escola Tècnica Superior d'Enginyeria de Camins, Canals i Ports
UPC BARCELONATECH

TRABAJO FINAL DE MÁSTER

LARGE TRIAXIAL TESTING ON REINFORCED GRAVELS

TRABAJO REALIZADO POR

Maxat Mamirov

DIRIGIDO POR:

Marcos Arroyo Alvarez De Toledo

Dr. Jong-Ryeol Kim

MÁSTER EN:

INGENIERÍA DEL TERRENO

Barcelona, **14 de junio de 2019**

Departamento de Ingeniería Civil y Ambiental

Abstract

Geogrids are parts of the geosynthetics that are used for soil reinforcement applications. One of the widely applications of the geogrid is a stabilization of unpaved and flexible pavement roads. Despite the field evidence that geogrid provides a good reinforcement of the pavement, all mechanical properties of the geogrid are not well studied. Several methods are used to evaluate the efficiency of the geogrid reinforcement including field tests, numerical modeling and laboratory test. A new large triaxial cell was designed to accommodate a specimen with dimensions of 300 mm in width and 850 mm in height, and 24 laboratory tests were conducted to investigate geogrid performance in two different coarse granular materials, one well graded and the other uniformly graded. The effect of two different types of geogrid were studied. Test results were analyzed to obtain peak strength and dilatancy effect of the samples. Moreover, the effect of grain size distribution on the peak friction angle was inspected.

Acknowledgements

I would like to express my deep gratitude to Dr. Marcos Arroyo and Dr. Jong-Ryeol Kim, my research supervisors, for their patient guidance, enthusiastic encouragement and useful critiques of this research work

I also thankful to faculty of and staff of Polytechnic University of Catalonia Civil Engineering Department for giving me opportunity to study master program and guiding and educating me during this period.

Table of Contents

List of Figures

List of tables

1. Introduction

1.1. Overview

This thesis includes a description of the research performed for the triaxial testing of gravels. The literature review covers the introduction to geosynthetic and particularly to geogrids, to main functions of the geogrid and to the application of geogrids in geotechnical engineering. In order to evaluate the efficiency of the reinforced gravel triaxial tests were performed. Two types of geogrids, with different properties, were used during laboratory testing. In addition, gravel was divided into two mixtures by grain size distribution. The thesis focuses on the testing procedure and obtained results for investigation of geogrids' effect.

1.2. Objectives

One of the principal objectives of the thesis is to carry out triaxial tests for the behavior analysis of reinforced and non-reinforced gravels. The results of each triaxial test will be provided. Moreover, the thesis will cover the comparison of the results obtained for two mixtures, which were reinforced by different types of geogrids. Thereby, the main purpose of this thesis is to analyze efficiency of the geogrids.

2. Literature review

Geosynthetics are defined as a synthetic or natural polymer manufactured product used in landfill works to overcome civil engineering problems. It can be used it a wide range of fields such as geotechnical, environmental, hydraulics, transportation and private development. Main functions of the geosynthetics are separation, reinforcement, drainage, filtration, etc. Geosynthetic can be subcategorized into geotextiles, geogrids, geonets, geomembranes, geosynthetic clay liners, geopipe, geofoam, and geocomposite (Koerner, 2005). They can be in the form of a sheet, strip or three-dimensional structure.

Geogrids are one of the types of geosynthetics that are growing in usage. Its structure consists of plastic rib forming equilateral triangular apertures as it can be seen in Figure 1. Due to its open-like structure, it can be used only for reinforcement and stabilization. Transverse and longitudinal ribs of the geogrids are manufactured from high-modulus polymers; therefore, the strength of geogrid ribs is higher than the strength of geotextiles.

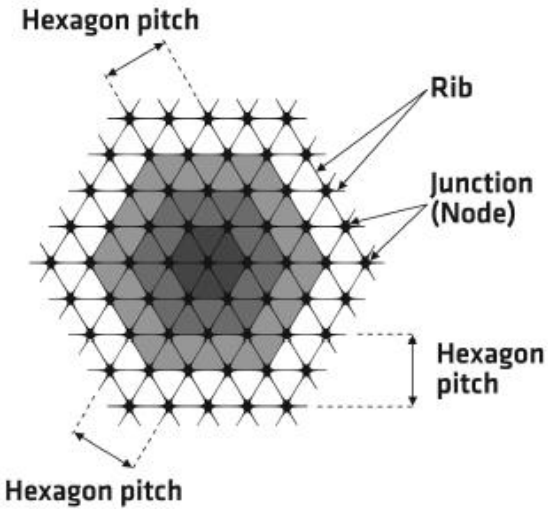

Figure 1. Grid reinforcement.

The applications of geogrids can be divided into main three categories: applications in road constructions, application in retaining walls, slopes and embankments, and application in foundation soils. Usage of geogrids in the construction of a road is to be described in the paragraph below.

2.1. Geogrid in unpaved roads

Main function of geogrid is reinforcement of the pavement. Geogrids traditional applications in pavement include subgrade stabilization, aggregate base reinforcement, and asphalt concrete reinforcement. For an application of the first two function described above, geogrid is required to be placed at the bottom layer of a pavement with thickness less than 14 in. Otherwise, when pavement layer thickness is greater than 14 in., the geogrid needs to be placed in the middle of the layer (Giroud, 2004).

A base layer of unpaved roads carries a great number of load applications where it acts as a permanent road. A surface rutting of 50-100 mm is frequently allowable for permanent unpaved roads if they can be easily reinforced by regrading. Nevertheless, huge rutting may cause a contamination of the base layer with subgrade soil, which may lead to loss of efficiency of base surface. Mechanisms that may lead to the surface rutting are:

- Compaction of base layer aggregate under cyclic traffic load
- Bearing capacity failure in base and subgrade soil from normal and tangential stresses caused by initial movement of traffic.
- Bearing capacity failure caused by deterioration of the base layer by subgrade soil.
- Accumulation of the incremental plastic strains caused by traffic load (Giroud, 2004).

The improvement of the subgrade material can be done by geogrids, which offers several mechanisms in preventing the surface rutting:

- Prevention of local shear of a subgrade. Small shear may occur in unreinforced roads because of vertical stress exceeding the elastic limit of road aggregate. The material of the base layer interrupts the subgrade, leading to the continuous deformation. Under the regular load, shear zones expand, the base deteriorates, vertical stress level grow, and superficial rutting appears. Finally, the limit plasticity or final bearing capacity of the subgrade is achieved which results in a full shear failure. A suitable reinforcement placed between the base and subgrade can help increase local shear and avoid deformation.
- Load distribution improvement. Increased load distribution and decreased normal stress acting on the subgrade are the expected improvements when roads reinforced by geogrid. Thereby, factor of safety due to bearing capacity rises.
- Decrease or reorientation of shear stress at subgrade. It is essential to realize that the shear stress occurred in the subgrade from base layer can be redirected inward or outward. According to the theory of plasticity, traffic loads produces outward shear stress which reduces bearing capacity, while geogrid creates an inward shear stresses that increase bearing capacity of subgrade.
- Tensioned membrane effect. Rutting at surface of the subgrade leads to the heaving when subgrade aggregate starts to shear. A geosynthetic placed at the interface forms wavelike shape that may be tensioned or stretched. When a flexible polymer takes a wavelike form, normal stress acting on a convex face is lower than normal stress at concave side. This action is named the “tensioned membrane effect” (Giroud, 2004).

2.2. Geogrid in flexible pavements

Three main mechanisms of reinforcement provided by geogrid are considered in this part. First mechanism is lateral resistant (Figure 2a) which restricts material from lateral flowing under applied load and leads to the growth of base shear strength. Consequently, vertical load distribution improves and vertical strain on the top of subgrade reduces (Zornberg & Gupta, 2010).

Second mechanism is described by movement of the failure envelope of the pavement to the new plane, which provides higher bearing capacity. Figure 2b illustrates the movement of the failure plane.

Tensioned membrane effect is considered as third mechanism (Figure 2c). It refers to the vertical stress distribution caused by tensile stress of a membrane.

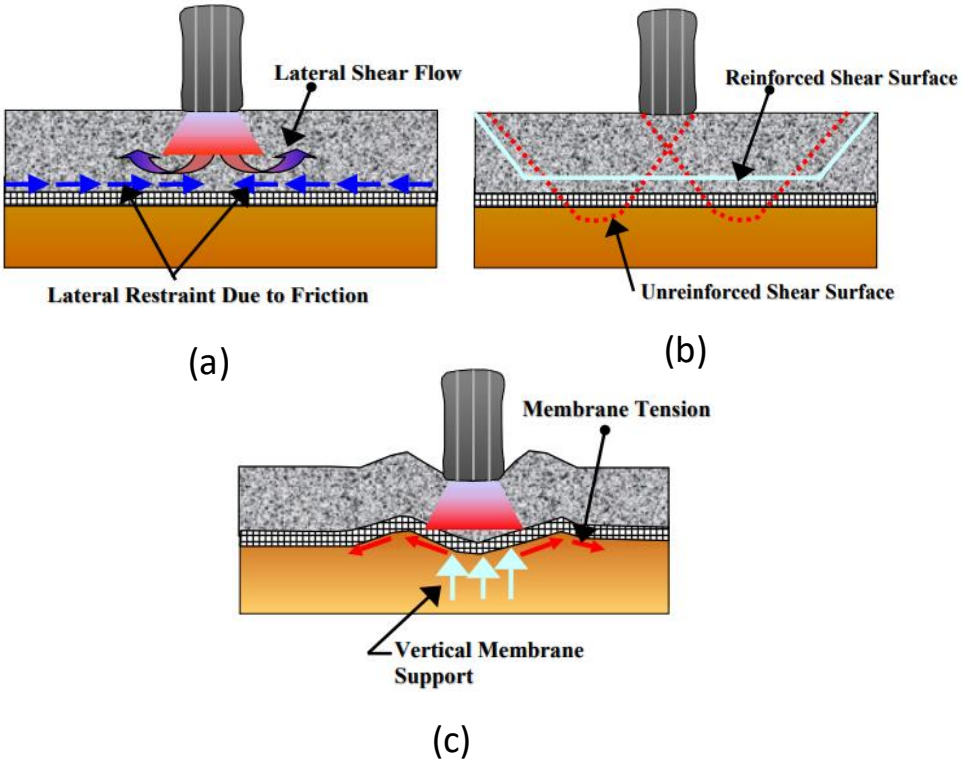

Figure 2. Reinforcement mechanisms: (a) lateral resistant mechanism, (b) improved bearing capacity mechanism, (c) tensioned membrane effect reinforcement (Haas, Walls & Carrol, 1988)

2.3. Geogrid in slope and wall reinforcement

This part considering an application of geogrids for slope and wall reinforcement.

The soil that is reinforced by the geogrid can be referred to the mechanically stabilized earth (MSE). Several reinforcement methods by mean of the geogrid are presented:

- Wraparound facing introduced as a soil-filled bags forming a facing of the slope and rest of the soil is behind the facing as a backfill. Furthermore, geogrid acts like a reinforcement in the backfill. This method is widely used for the walls and slopes at the angle up to 80 and with height variability from 3 m to 50 m.
- Timber facing refers to geogrid located between timbers and held by friction and/or when geogrids tied to large timbers by batten strips.
- Articulated precast concrete panels compose of the precast concrete panel with entry for the geogrids.
- Full height precast panels are structures of concrete panels acting like a reinforcement prior to backfill works are finished.
- Cast in place concrete panels are walls with wraparound geogrids which are covered by panels.

- Gabion facing represent a box filled with rocks or soil and reinforced by geogrid, which are placed between boxes.
- Welded wire-mesh facings similar to gabion facings, but with no rock fills.
- Masonry block faced walls at which geogrid is placed between the blocks and held by friction (Chen, Zhang & Li, 2014).

3. Methods of studying geogrid reinforcement

3.1. Field testing

Experimental studies have been found as one the methods for analysis of geogrid reinforcement. They include testing of in-situ soil and geogrid. Experimental studies can be subdivided into field and laboratory testing. Field testing is providing an in-situ studies of the geogrid reinforcement. Forex ample, observation of the unpaved road reinforcement can be done within road. Furthermore, the field test includes full-scale experiments which shows natural behaviour of the reinforced soil. However, the cost of data collection is high including unstable weather conditions; thus, leads to the limited amount of field tests (Indraratna, Salim & Rujikiatkamjorn, 2011)

3.2. Numerical studies

The most commonly used methods for numerical studies are the finite element methods (FEM) and the discrete element method (DEM). Generally, numerical methods require a deep knowledge in the behaviour and the interaction between various materials like asphalt, base course, subgrade, geosynthetic reinforcement. Moreover, current analytical tools are unable to predict the time-dependent behaviour of roads under real traffic load.

3.3. Laboratory testing

There are great number of laboratory test aimed on the study of mechanisms of reinforced soil, in particular, reinforced flexible pavement. Based on the used method, the laboratory tests are categorized into: confined and unconfined tests. According to Mehrjardi e t. (2016), properties of geogrid in confined laboratory test are measured in the soil confinement, while unconfined laboratory test studies properties in-air. As the geosynthetics in the base soil of pavements are subjected to the confined conditions, only confined tests will be considered.

Geogrid placed in the base layer confined by soil under cyclic traffic load. The confinement of soil around geosynthetics is dependent on macroscopic properties and structure of geosynthetics, soil

properties, and on soil-geogrid interaction. Triaxial cells are designed for confined laboratory testing of soils, however the inclusion of geogrids requires large equipment and therefore there are very few examples of triaxial testing that includes geogrids (Chen et al. 2014).

4. Equipment description

4.1. Triaxial cell

Following a previous design by Alvarado (2017) a large triaxial cell was newly commissioned) for the Geotechnical Laboratory at UPC to accommodate specimen with dimensions of 300 mm diameter and 850 mm height. The cell is made of the 316 stainless steel parts. Main parts of the cell are: 1) a cylindrical chamber, which is open from the both ends and contains slots for screws; 2) a base in which chamber stands, with porous pedestal that can saturate the specimen if required; 3) the lid with an axial opening to guide the axial loading assembly; 4) the axial loading assembly that applies axial load to the sample. All parts that described above are bolted together and impermeability of the system is ensured by acrylonitrile-butadiene O-rings. Internal pressure of the chamber can be increased up to 800 kPa. An overall view of the triaxial cell is shown in Figures 3 and 4.

Figure 3. Main parts of the triaxial cell.

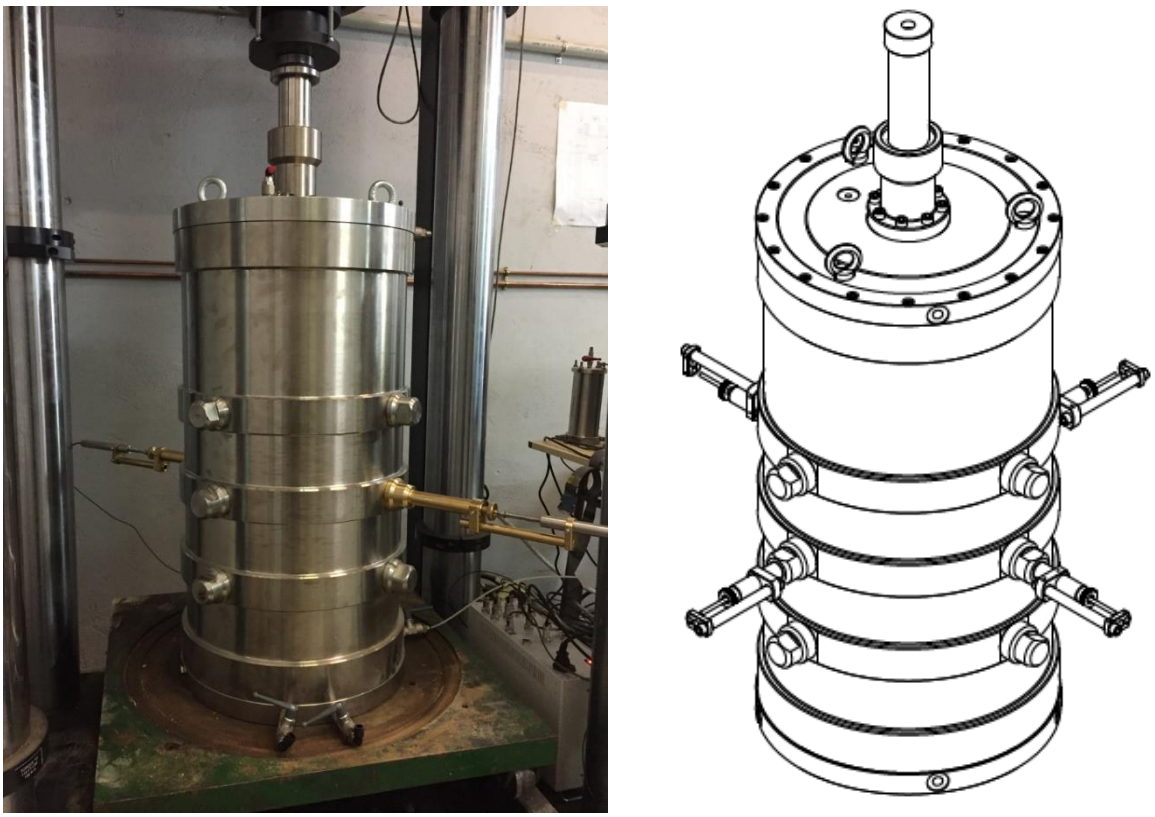

Figure 4. Mounted Triaxial cell.

4.2. Loading system

Axial load is applied by an Instron press (Model: 223925-2), which has capacity of 2000 kN and can be manipulated either by displacement or load control. Frame (Figure 5) has a crosshead adjusted and secured with hydraulic crosshead lift and lock cylinders that is referred to the J3-Style Crosshead (Instron, 2009). J3-Style Crosshead allows to move the crosshead along the frame, which gives a great number of testing variabilities. Testing speed range is 0.1 to 203 mm/min. Power supply for the frame comes from the hydraulic power supply (HPS) (Figure 5) which produces different hydraulic pressures as required. Main components of the HPS are: a reservoir; a pump; an electric motor; a heat exchanger; one or more manifold assemblies; and the hydraulic fluid (oil). HPS is connected to the PC and control panel.

Figure 5. Instron press frame HPS and control panel.

Cell confining pressure is delivered from the laboratory compressor air system circuit, maintained at 1 MPa. A pressure regulator, manufactured by Fairchild Industrial Products company (Model 4000), has maximum output pressure of 1000 kPa and controls chamber pressure. In addition, as it can be seen on Figure 5 system includes a transitional container, which provides a connection between pressure regulator and chamber. Schematic representation of the air supply system can be seen in Figure 7.

Figure 6. Compressed air supply system, pressure regulator and transitional container.

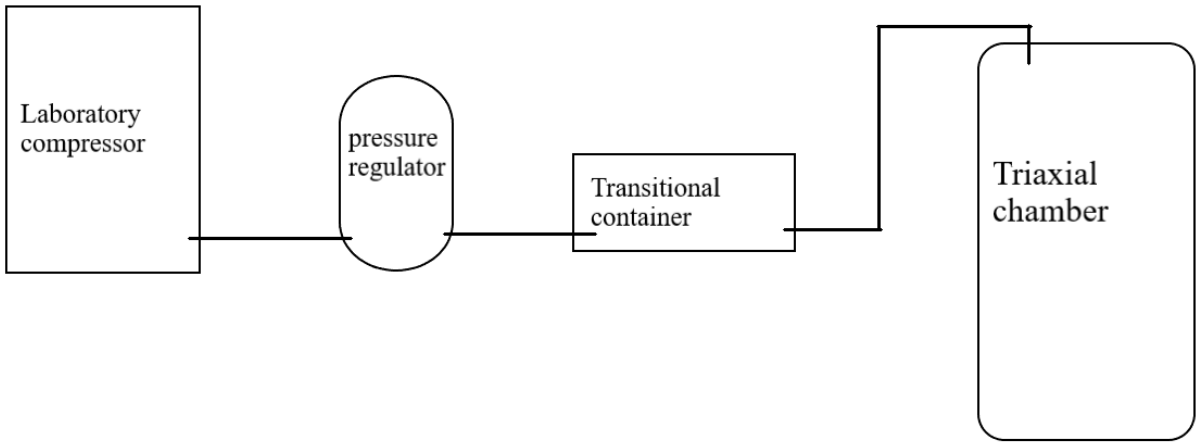

Figure 7. Schematic representation of air supply system.

4.3. Instrumentation

4.3.1. Frame load measurement system

Press has a strain gauged load cell that measures applied force to the test sample. The load cell (14, Figure 8) is mounted to the end of the rod (10). Such installation of the components separates a load measuring system from the hydraulic system. This mean that the force measured by the load cell cannot be affected by the piston friction and hysteresis, consequently, it is a direct force measurement.

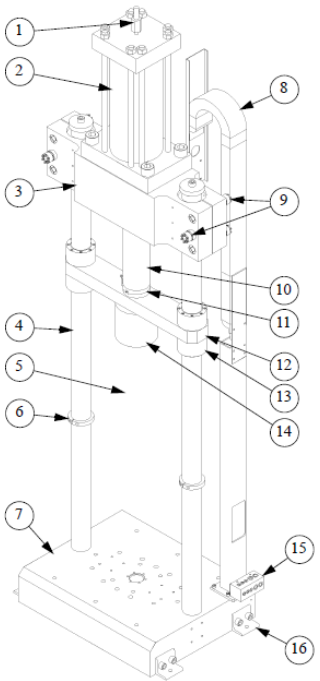

Figure 8. Frame components.

4.3.2. Frame displacement measurement system

Vertical displacement of the piston inside of the hydraulic cylinder is measured by a position encoder. This model has a magnetostrictive-type encoder which is mounted to the stationary end of the hydraulic cylinder (Figure 9). The encoder rod extends through the hydraulic cylinder and piston, so when piston moves up or down, the encoder magnet moves along the encoder rod. Magnet produces an electrical signal that records exact position of magnet on the encoder rod. The electrical signal is transmitted to an I-Series control unit, which is installed near main computer. The I-Series control unit converts the signal to the absolute position of the crosshead in relation to a stationary frame member (Instron, 2009). Measurement error is +/- 0.13 mm or 0.1 % of displayed reading.

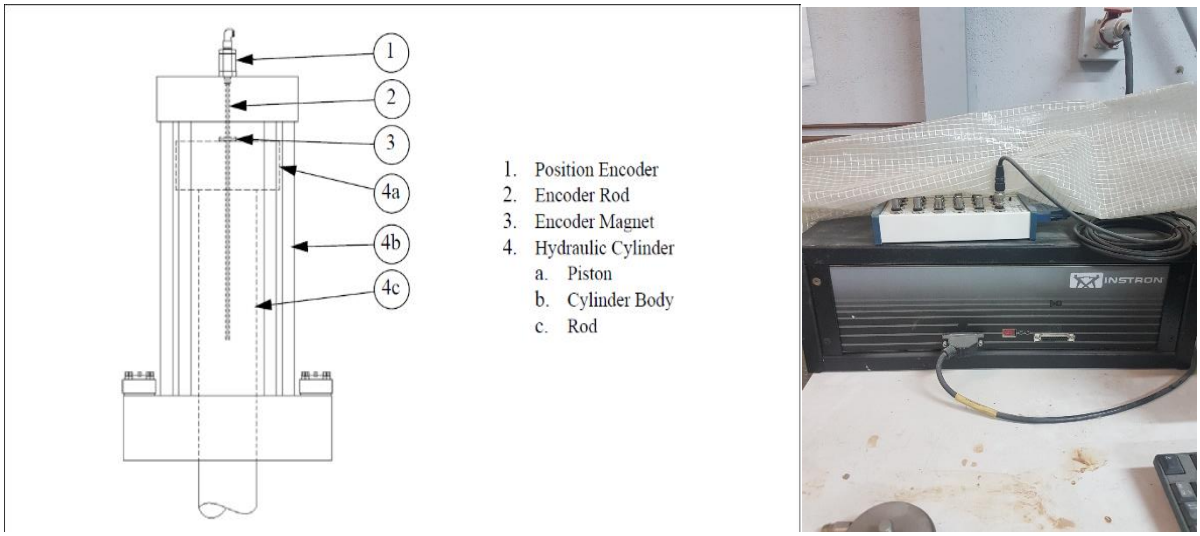

Figure 9. Magnetostrictive-type encoder and I-series control unit.

4.3.3. Pressure measurement system

Chamber confining pressure measurement is done using a piezoelectric pressure sensor which is connected to the transitional container from one side and on the other hand is connected to the data acquisition panel (Figure 10). Pressure sensor is produced by RS company with serial number 461-367. Range of the measuring sensor is from 0 to 40 bar with an output between 0 to 5 volts and reading accuracy of +/- 0.25%. Data acquisition panel is connected to the PC with the preinstalled GeoLab software that records all readings.

Figure 10. Piezoelectric pressure sensor and data acquisition panel.

4.3.4. Radial displacement measurement system

Radial displacement is measured by linear inductive displacement transducers (LVDT's) (Figure 11). Power supply and ADC conversion is done through the data acquisition panel.

Figure 12 represents a probe that are made of brass and include two main parts: a guide cartridge that is threaded through the triaxial cell wall and one internal rod housed in the cartridge. At the internal end of the rod a radial disk contacts the membrane, whereas at the external end LVDT's is placed (Figure 11). Both ends are joined by a splice which in turn serves as a stop for a spring that provides adequate stiffness to the sensor and is regulated with a nut threaded to the guide cartridge. The entire system is designed so that the radial probe disk always remains in contact with the sample, in this way, when there is radial deformation, the spring allows a rigid body displacement of the rod and end disks, which is continuously registered by means of the displacement transducer. The spring used is a rectified compression spring, with the following specifications: 77mm in length, 10mm external diameter, 1.70mm thickness and an elastic constant k=6N/mm.

Figure 11. Linear inductive displacement transducer (LVDT's).

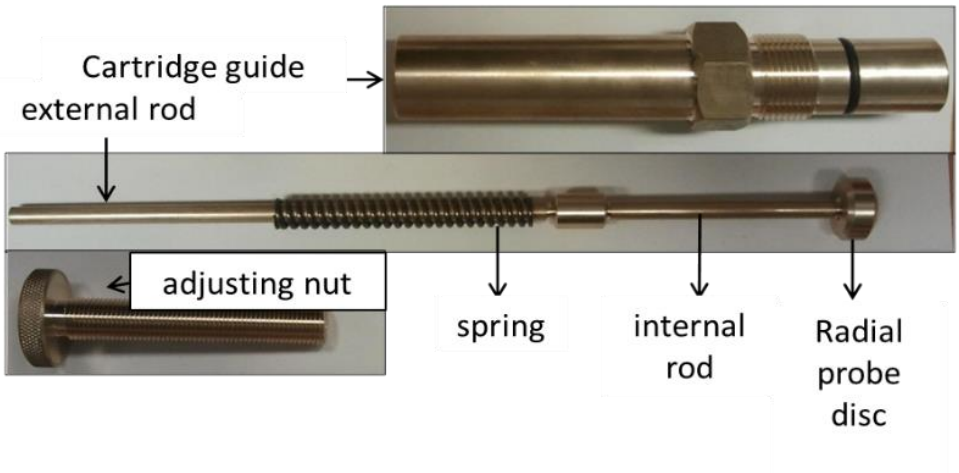

Figure 12. Probes for local radial measurement.

4.4. Data acquisition and control

The Instron press is operated through its own inbuilt software, Bluehill. The user needs to select test method and modify the control mode (e.g. stress or strain control), stress path, including un-loading and cycles, initial conditions of the specimen, and loading rate. During the consolidation stage the maximum load should be specified. As it mentioned above HPS and I-Series control unit are connected to the main PC, and records any movements of the frame.

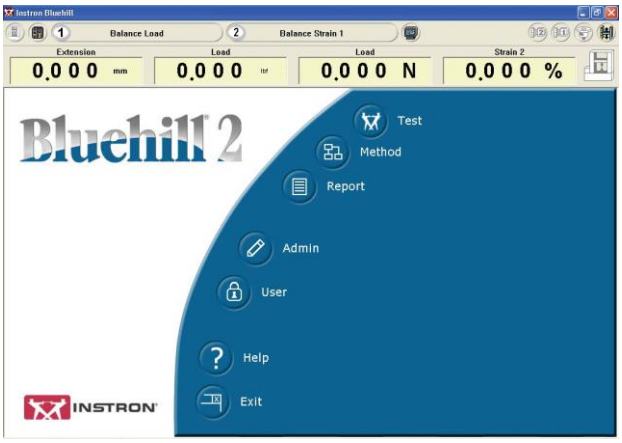

Figure 13. Bluehill software.

GeOLab software us used to record measured pressure changes and radial displacement, the software is installed in a dedicated PC positioned near the frame as showed in Figure 14. This software does not require any input, as it only acts like a reading unit.

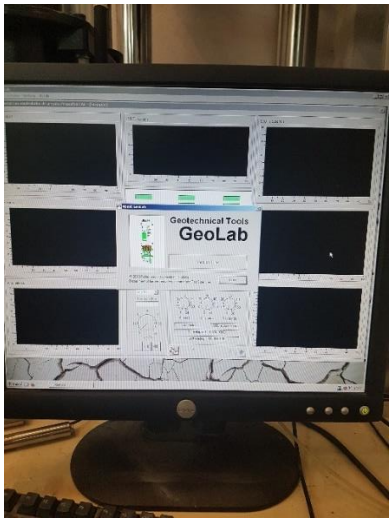

Figure 14. GeoLab software.

4.5. Auxiliary equipment

The specimen membranes were specifically ordered for the triaxial testing procedure. Membranes are made of the styrene-butadiene in a single piece without joints, and anti-abrasive surface coating. They have an initial internal diameter of 280 mm, thickness 4 mm and Young Modulus E ≈ 38 kg/cm^2.

The auxiliary equipment includes: a crane consisting of a rotating boom, a hoist with a capacity to support 9.8 kN; one platform for mounting the specimen and another that helps position the mounted cell into the press, and two compaction hammers.

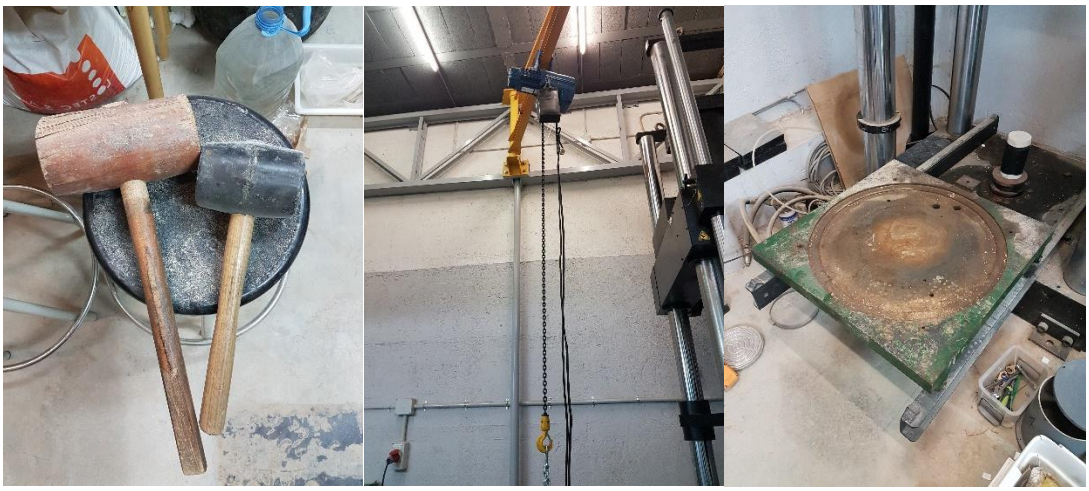

Figure 15. Auxiliary equipment.

Furthermore, during the testing procedure compacted hammers were replaced by the Standard Proctor hammer (Figure 16) that meets ASTM D558 specification. It has a 2.54 kg weight and a drop of 305 mm with a diameter of 50 mm. In order to distribute applied force by the Proctor hammer wooden plate were placed between sample and hammer.

Figure 16. Standard Proctor hammer and wooden plate.

5. Materials

5.1. Granular material

For the triaxial testing granitic gravel was selected as a granular material. Gravel has a maximum grain size of 25 mm and was brought from nearby quarry. Material with grain size distribution from 0 to 25 hereafter referred to “Mixture 0/25” and material between sizes 10 and 25 mm referred to “Mixture 10/25”, two different mixtures are shown in Figure 17.

Figure 17. Mixture 0/25 and 10/25.

The grain size distribution (GSD) curves of these materials are represented in Figure 18. In addition, by interpolating the data from the GSD graph granulometric properties were obtained and summarized in Table 1. According to the EN ISO 14668-2 Mixture 0/25 is classified as a well graded soil and Mixture 10/25 is uniformly graded soil.

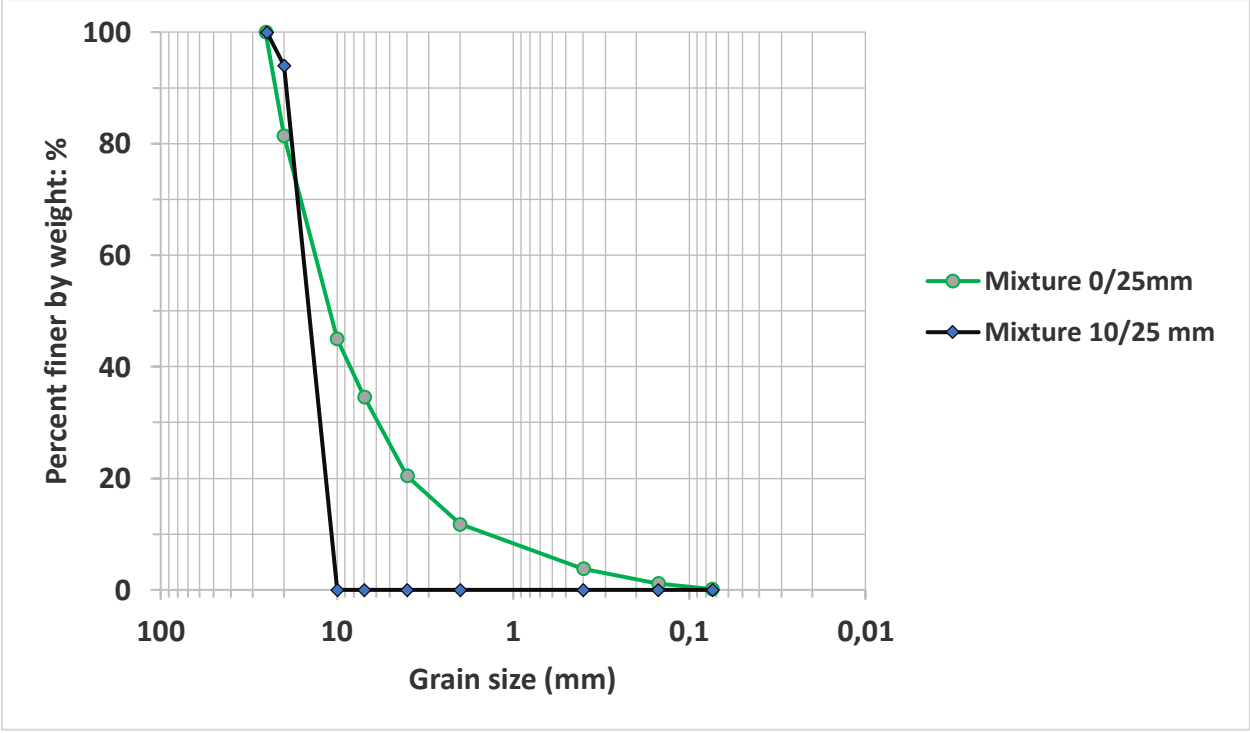

Figure 18. Grain size distribution of Mixture 0/25 and 10/25.

Table 1. Granulometric properties of mixtures.

Grain size distribution	D_{10}	D_{30}	D_{60}	C_c	C_u
Mixture 0/25	1.60	5.90	14.15	1.53	8.84
Mixture 10/25	11.15	14.2	17.50	1.03	1.57

It was verified that the fines in Mixture 0/25 were not plastic. Other physical properties of the mixture (e.g. water absorption < 1 %; density of particles: 2.70 Mg/m^3) are reported in the quarry data sheet, Figure 19.

Mixture 10/25 was creating by following recipe: a) removing all sizes below 10 mm sieve and larger 25 mm sieve; b) extract 20% by weight of the retained material greater than 20 mm sieve; c) extract 80% by weight of the retained material greater than 10 mm sieve. Detailed table will be given in section Testing procedure.

FICHA TÉCNICA **R 07.4 A**

CANTERAS CANRO, S.A.
BV-5001 – Ctra. de la Roca, Km. 10
C.P. 08105 SANT FOST DE CAMPSENTELLES
BARCELONA

CE
09
CANTERAS CANRO, S.A.
NºA004.00-151110

EN 13242:2002+A1:2007 ARIDOS PARA CAPAS GRANULARES Y CAPAS TRATADAS CON CONGLOMERANTES HIDRÁULICOS PARA USO EN CAPAS ESTRUCTURALES DE FIRMES

NOMBRE COMERCIAL	TAMAÑO		CÓDIGO	
TODO UNO 0/25 mm	0/31,5		AG-T-0/31,5-G	
REQUISITO	**VALOR**	**UNIDADES**	**CATEGORÍA**	**PROCEDIMIENTO DE ENSAYO**
Tamaño de las particulas	0/31,5	d/D		EN 933 - 1
Granulometria	DECLARADA		$G_A80\ GT_A25$	EN 933 - 1
Contenido de finos			f_9	EN 933 - 1
Equivalente de arena SE4	>35	%	valor informativo	EN 933 - 8
Azul de metileno	<10	g/Kg	valor informativo	EN 933 - 9
Densidad particulas	2,70	(g/cm³)	valor declarado	EN 1097 - 6
Absorción de agua	<1	%	valor declarado	EN 1097 - 6
Caras de fractura			$C_{90/3}$	EN 933 - 5
Indice de lajas			FI_{35}	EN 933 - 3
Resistencia a la fragmentación			LA_{30}	EN 1097 - 2
Desgaste Microdeval	N.P.D.			EN 1097 - 1
Durabilidad : Sulfato magnésico			SM_{18}	EN 1367 - 2
Sulfatos solubles en ácido			$AS_{0,2}$	EN - 1744 – 1 Apdo 12
Azufre total			S_1	EN - 1744 – 1 Apdo 11
Humus	Exento	%	valor declarado	EN - 1744 – 1 Apdo 15.1
Reactividad álcali-sílice	No reactivo		valor declarado	UNE 146507-1 EX.
Sustancias peligrosas	N.P.D.			
Estudio petrográfico	A.1.1.3 Roca Ígnea Plutónica: GRANODIORITA. COMPOSICIÓN MINERALÓGICA CUARZO 45 % FELDESPATO POTÁSICO 15 % PLAGIOCLASA 25 % BIOTITA 15 % MOSCOVITA < 1 %			UNE - EN 932-3

Figure 19. Technical quarry description of Mixture 0/25.

5.2. Geogrid

Two rolls of geogrid, which belong to the TriAx series, were delivered to the laboratory. TriAx are made of a stiff polymer which produces a hexagonal geogrid structure (Figure 20). Moreover, geogrid consisting of junctions and stiff ribs which forms equilateral triangular apertures. Such structure of the geogrids stabilizes granular material by partially interlocking aggregates between the ribs. This mechanism results in confinement and lateral resistant of the granular particles (Lees, 2017).

Figure 20. Geogrid junction and rib.

Two types of the geogrid were selected for the further testing procedure. From this point forward they will be referred as Tx150 and Tx170 (Figure 21). Characteristics and main difference of the geogrids are represented in Table 2. Specifications were taken from the official website of the distributor of the geogrids.

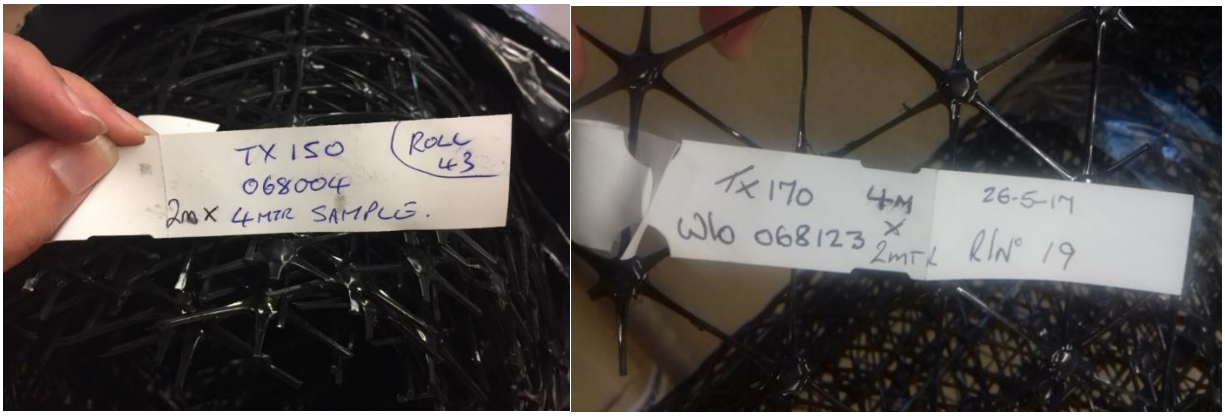

Figure 21. Geogrid identification tags.

Table 2. Characteristics of the geogrids.

Geogrid type	Radial secant stiffness at 0,5% strain (kN/m)	Radial secant stiffness ratio	Junction efficiency (%)	Hexagon pitch (mm)
TX150	360	0,80	100	80
TX170	480	0,80	100	80

6. Testing procedure

6.1. Experimental program

The experimented program reported here includes twelve tests on the Mixture 0/25 and twelve tests on Mixture 10/25 in dry conditions. Table below summarizes the tests conditions. Test without geogrids hereafter will be named as without geogrid or NG. Geogrids where placed in the

middle of the sample, approximately at high 280-320 mm from the bottom. All tests include an initial phase of isotropic compression and then a second phase of shear under constant radial stress. The purpose of this test series was to obtain an independent set of data to verify the good performance of the newly commissioned larger cell.

Table 3. Summary of the tests performed.

Grain size distribution	Reinforcement situation	Confining pressure (kPa)	Number of tests
Mixture 0/25	Without geogrid (NG)	75, 120, 160, 200	4
	TX150[(1)]	75, 120, 160, 200	4
	TX170[(1)]	75, 120, 160, 200	4
Mixture 10/25	Without geogrid (NG)	75, 120, 160, 200	4
	TX150[(1)]	75, 120, 160, 200	4
	TX170[(1)]	75, 120, 160, 200	4
[(1)] Located in the middle of the sample			

6.2. Testing procedure

6.2.1. Material preparation

Approximately 70 kg of granular material is needed to create a triaxial specimen for the large 300 mm cell. The granular material, which is initially stored outside the laboratory building in bulk bags, is transferred to the laboratory in batches totaling around 180 kg. The batches are extended in the storage section of the laboratory floor and allowed to fully dry at room temperature (Figure 22). After drying the granular material sample is divided into four batches of equal mass and transferred to the laboratory where the testing equipment is located.

Figure 22. Granular material transferred and drying.

To create Mixture 10/25 dried granular material was sieved in the sieving machine before proceeding to the test. High capacity sieve shaker (Figure 23) was used to sieve approximately 115 kg of the granular material. It was observed that to create a sample with Mixture 10/25 with height of 520 mm, 47 kg of the granular material will be needed.

Figure 23. High capacity sieve shaker.

Discs of approximately 28 cm diameter are cut from the geogrid rolls to prepare for insertion in the triaxial specimen. In addition, tips of the geogrid were melted to avoid puncturing of membrane during the test.

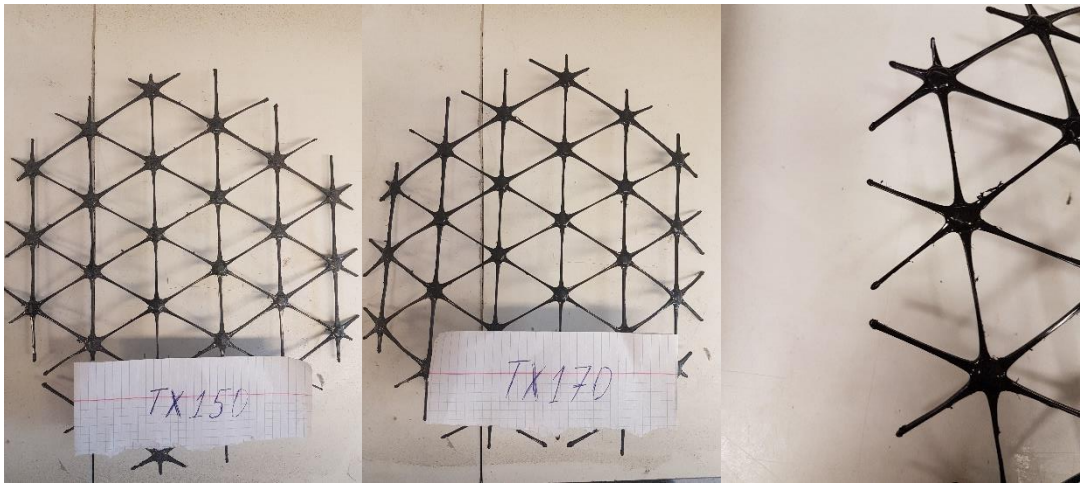

Figure 24. Cutted geogrid and melted tips.

6.2.2. Specimen preparation

Specimen preparation starts by fastening the membrane to the base of the triaxial cell with a hose clamp (Figure 25). To avoid breakage of the membrane by indentation an additional layer of rubber, 2 mm in thickness, is placed between the clamp screws and the membrane.

Figure 25. Membrane mounting.

A light compaction procedure was desired to mimic the situation of coarse granular materials on unpaved roads and railtrack. The granular material placed inside the membrane in 4 layers, of approximately 140 mm height each, to reach a final height of between 550 and 575 mm. The material is initially loaded inside the membrane with a shovel. Each layer is then lightly compacted using a procedure that includes 40 vertical hits with a crowbar and 80 radial hits by hand-held

rubber and wood hammers. When the test specification includes a geogrid, it is placed between the second and the third granular layers at height of 250-280 mm (Figure 26).

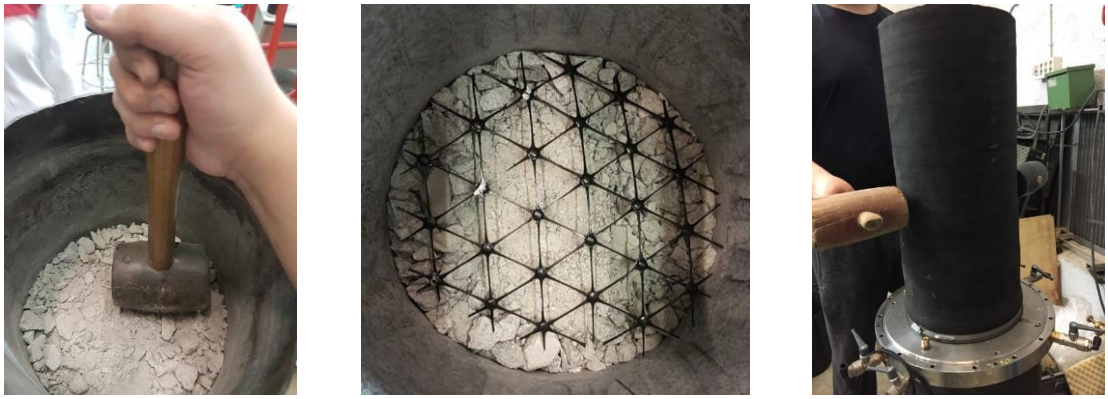

Figure 26. Material placement and compaction.

The procedure just describes was observed to result in too variable initial densities. In view of this, compaction procedure was changed and included the usage of the Standard Proctor hammer and wooden plate. After loading of each layer wooden plate was placed on the top of the layer and 15 blows by the Proctor hammer were performed. The energy supplied for compaction process equals to 14 kJ/m^3, which is 2% of the Standard proctor energy referenced by ASTM D 698. Thereby, compaction process was stabilized and made a height of the specimens approximately equal. Compaction procedure was changed after tests on Mixture 0/25 with geogrid Tx150.

Figure 27. Compaction procedure by Standard Proctor hammer and wooden plate.

After all four layers are compacted inside of the membrane, the specimen is closed by the porous cap. In the same to avoid air penetration inside of the sample during triaxial test cap is fixed by hose clamps (Figure 28).

Figure 28. Closing specimen.

At this stage the cell is transported by the crane and connected to the triaxial base using sixteen bolts. The local radial LVDT are inserted in the middle of the cell, at height of 380 mm above the ground, and adjusted. It is carefully verified that the radial probe disc is in contact with the membrane. Then cell is closed by the top cap with piston which, similarly to the bottom part, is fixed to the cell wall by sixteen bolts. At this stage the triaxial cell is ready and can be moved into the press. Once the triaxial cell is under the press, air pressure hose is connected to the top of the lid as indicated in Figure 29. Note the positioning of the geogrid, slightly below the radial transducers, to avoid problems such as those described in the next section.

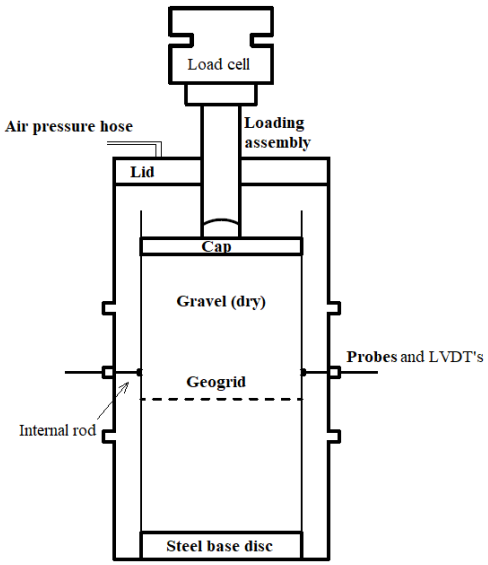

Figure 29. Closed large scale triaxial cell.

The press ram is lowered down to achieve contact with the cell piston, at which point all the press transducers are zeroed.

In order to connect LVDT's, they placed inside of the system of local radial measurement and tighten. Using GeoLab software LVDT's adjusted so that measured value tends to zero. Moreover, pressure must be set up to desired value by regulator. Finally, an isotropic compression phase is launched. The isotropic load is ramped in 2 min. It follows a creep phase (at maintained isotropic load) of 3 hours; finally, the shear compression phase lasts 1 hour. The aim of the first stage of the triaxial test is to consolidate the sample to set a base for further evaluation. While during the shearing phase of the test stress-strain, deformation of volume or pore pressure relations are determined (Poul, 2016)

Applied load and the rate during the isotropic consolidation stage can be calculated by following equations:

$$L = p * \pi * \frac{D^2}{4} \ [N]$$

$$v_1 = \frac{L}{2} \ [N/min]$$

Load of the press depends on the applied pressure (p, N/mm^2) and diameter (D, mm^2) of the piston of the triaxial equipment. Further, calculated load should be reached in 2 minutes, which gives us load velocity (v_1, N/min) during first phase of the test.

For the shear compression phase, it is desired to obtain 20% of axial deformation (ε_a, mm) in one hour. Axial deformation can be calculated by interpolating height (h, mm) of the sample. Next, load velocity (v_2, mm/min) during the second stage can be achieved.

$$\varepsilon_a = h * 0.2 \ [mm]$$

$$v_2 = \frac{\varepsilon_a}{60} \ [mm/min]$$

6.3. Problems observed and limitations

The main difficulty observed during testing has been derived from damage caused by the geogrid to the equipment:

- In several instances the geogrid tips (Figure 22) have punctured the 4 mm thick membrane during the isotropic pressure ramp.

- In two instances the geogrid has contacted one of the radial transducers, acting as a hard point and resulting in bending of the transducer internal rod (Figure 10).

The second problem required recommissioning of the radial transducers. To avoid its recurrence, the thickness of the second compacted layer has been slightly readjusted so that the geogrid is now left a few mm below the contacting points of the radial transducers (see Figure 29).

The puncturing of the membranes was initially addressed by repairing the membranes with adhered layers of extra rubber (Figure 30) but kept on happening. Furthermore, membrane manipulation resulted in small creases (Figure 31) that manifested themselves in diminished cell tightness and loss of confinement (the air pressure leaking inside the membrane). Problem of creases was solved by covering them with vinyl spray, forming a thin layer of vinyl that fills creases, as illustrated in Figure 31. After many trials, (including local modification of the grid tips by burning) it was observed that the problem of puncturing only could only be avoided by limiting cell confinement to 200 kPa and slightly shortening the diameter of the grid disk inserted to about 25 cm.

Additionally, axial loading assembly (piston) was scratched after several tests (Figure 28), consequently, when piston was reaching certain point leakage of air started to appear. Therefore, required axial deformation of 20% was not achieved, maximum axial deformation that could be achieved varied from 7% to 12% depending on the initial height of the sample. However, these limits did not effect on velocity calculations for the shear phase.

In several cases internal rods of the probes (Figure 12) got stuck by the weight of the material, thus led to the breakage of the membrane and deformation of the internal rod (Figure 30). The problem was solved by changing internal rod to the new one and repairing membrane with additional layer of rubber.

Figure 30. Repaired part of membrane, scratch on piston and deformed internal rod.

Figure 31.Creases and vinyl layer.

7. Experimental results

7.1. Initial conditions

The initial properties of the tested samples are summarised in Table 4 and Table 5. The initial water content for all specimens is 0.6%. The light compaction procedure resulted in variable yet relatively loose specimens. Those specimens in which a grid was placed had smaller densities on average that those in which no grid was present. Initial dry density depends of the initial height and the weight of the sample. Initial void ratio (e) was expressed in terms of specific gravity (G_s, Mg/m^3) and dry density (ρ_d, Mg/m^3) of the sample, and calculated by given equation:

$$e = \frac{G_s}{\rho_d} - 1$$

Table 4. Initial conditions for Mixture 0/25.

Test name	Granular Material	Grid	Confining pressure at shear (kPa)	Initial dry density (Mg/m^3)	Initial void ratio
Mx0/25_75_NG	Mixture 0/25	No	75	1.773	0.51
Mx0/25_120_NG	Mixture 0/25	No	120	1.880	0.42
Mx0/25_160_NG	Mixture 0/25	No	160	1.818	0.48
Mx0/25_200_NG	Mixture 0/25	No	200	1.819	0.47
Mx0/25_75_150	Mixture 0/25	Tx150	75	1.787	0.58
Mx0/25_120_150	Mixture 0/25	Tx150	120	1.781	0.50
Mx0/25_160_150	Mixture 0/25	Tx150	160	1.810	0.48
Mx0/25_200_150	Mixture 0/25	Tx150	200	1.660	0.61
Mx0/25_75_170	Mixture 0/25	Tx170	75	1.768	0.50
Mx0/25_120_170	Mixture 0/25	Tx170	120	1.768	0.50
Mx0/25_160_170	Mixture 0/25	Tx170	160	1.762	0.50
Mx0/25_200_170	Mixture 0/25	Tx170	200	1.799	0.47

As it can be seen from Table above initial void ratios are varies for the first eight tests which were compacted by the rubber and wooden hammer procedure. Averaged value of initial void ratios for Mixture 0/25 is equal to 0.50, As the compaction procedure was changed to the Standard Proctor hammer initial densities of the sample has been observed to be approximately equal.

Table 5. Initial conditions for Mixture 10/25.

Test name	Granular Material	Grid	Confining pressure at shear (kPa)	Initial dry density (Mg/m^3)	Initial void ratio
Mx10/25_75_NG	Mixture 10/25	No	75	1.393	0.90
Mx10/25_120_NG	Mixture 10/25	No	120	1.395	0.90
Mx10/25_160_NG	Mixture 10/25	No	160	1.415	0.87
Mx10/25_200_NG	Mixture 10/25	No	200	1.414	0.87

Mx10/25_75_150	Mixture 10/25	Tx150	75	1.407	0.88
Mx10/25_120_150	Mixture 10/25	Tx150	120	1.418	0.87
Mx10/25_160_150	Mixture 10/25	Tx150	160	1.415	0.87
Mx10/25_200_150	Mixture 10/25	Tx150	200	1.424	0.86
Mx10/25_75_170	Mixture 10/25	Tx170	75	1.423	0.86
Mx10/25_120_170	Mixture 10/25	Tx170	120	1.424	0.86
Mx10/25_160_170	Mixture 10/25	Tx170	160	1.416	0.87
Mx10/25_200_170	Mixture 10/25	Tx170	200	1.420	0.87

Since the procedure of compaction for the Mixture 10/25 was done by a Standard Proctor hammer, initial void ratios of the sample are in the range between 0.86 to 0.90, in average 0.86. By comparing initial conditions of two mixtures we can observe expected decrease of the dry densities and increase of the void ratios.

Youd (1973), proposed a plot of variation of maximum and minimum void ratios with the coefficient of uniformity and angularity. It was assumed to use angularity, which is related to the shape of the soil, equal to 0.3 since it is closet fit to the obtained void ratios. As a result, it is observed that the void ratios obtained for Mixture 0/25 and Mixture 10/25 are approximately equals to the maximum void ratio at given coefficient of uniformity. It appears then that the applied energy by proctor hammer, which is only 2% of the standard energy, is conducive to obtain void ratio cose to the conventional maximum.

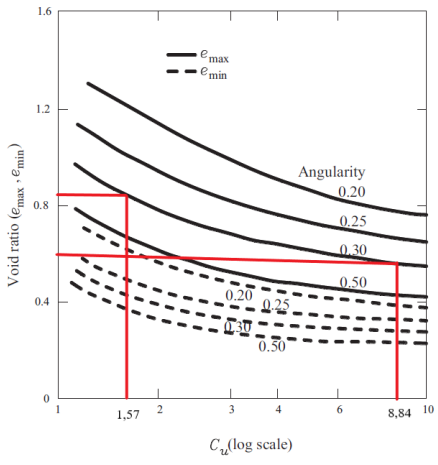

Figure 32. Variation of e_{max} and e_{min} with C_u and angularity (Youd, 1973).

7.2. Test results

In this chapter plots of deviatoric stress q against axial strain ε_a at different confining pressures for two different mixtures are presented and compared. Due to the limitations described in section 5.3, for Mx0/25 it was chosen to present results at 9% of axial deformation while results for Mx10/25 were presented at 7% axial deformation. Volumetric strain ε_v against axial strain ε_a plots are also presented for each test to observe dilatancy and volume change of granular material during the shear phase.

Additionally, graphs of void ratio e versus mean stress p' during isotropic compression phase were included to present granular material behaviour. Results for strength envelope in the Cambridge plane were presented at ultimate conditions of axial deformation for each test. The strength envelope is presented in the Cambridge plane, using the stress variables:

$$p = \frac{\sigma_a + 2\sigma_c}{3}$$

$$q = \sigma_a - \sigma_c$$

A linear envelope has been fit through the results, forcing a zero intercept and peak friction angle φ' was derived from the relationship with slope M:

$$M = \frac{6 \sin \varphi'}{3 - \sin \varphi'}$$

It is assumed that the deformed shape of the sample after the shear phase is as illustrated in Figure 34.

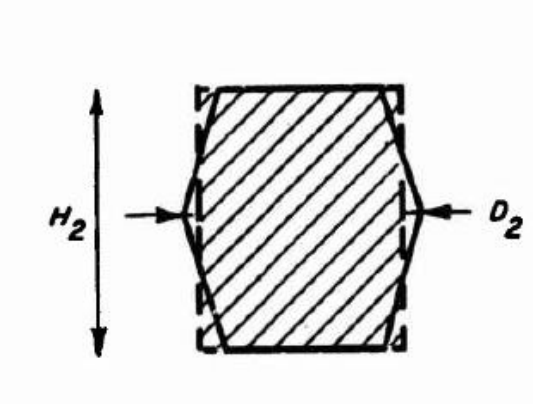

Figure 33. Cross section of assumed deformed shape.

For this type of deformation Ehrgott (1971) suggested following formulas:

$$\varepsilon_a = \frac{\Delta H}{H_o}$$

$$\varepsilon_r = \frac{\Delta D}{D_o}$$

Where, ε_a axial strain, ε_r radial strain, H_o and D_o are initial height and diameter respectively, and ΔH and ΔD are height and diameter changes.

Thus, volumetric strain deformation can be calculated by:

$$\varepsilon_v = \varepsilon_a - 2 * \varepsilon_r$$

7.2.1. Mx0/25_NG

The deviatoric stress was calculated from the recorded axial load taking into account load corrections which were made since recorded values in Bluehill software were negative. Following Alvarado (2017) membrane penetration corrections were not considered necessary because of the membrane very stiff nature.

Plots of deviatoric stress against axial strain at different confining pressures for Mx 0/25_NG are shown in Figure 34. An appropriate increase of the deviatoric stress was obtained. By comparing tests at 160 kPa and 200 kPa confining pressures, it can be seen that test with higher confining pressure had a lower deviatoric stress in the beginning, probably due to poor compaction during the sample preparation. Moreover, on Figure 35 void ratio changes during the isotropic compression phase are represented, where compaction of the test Mx0/25_200kPa_NG was smaller in comparison with the test Mx0/25_160kPa_NG.

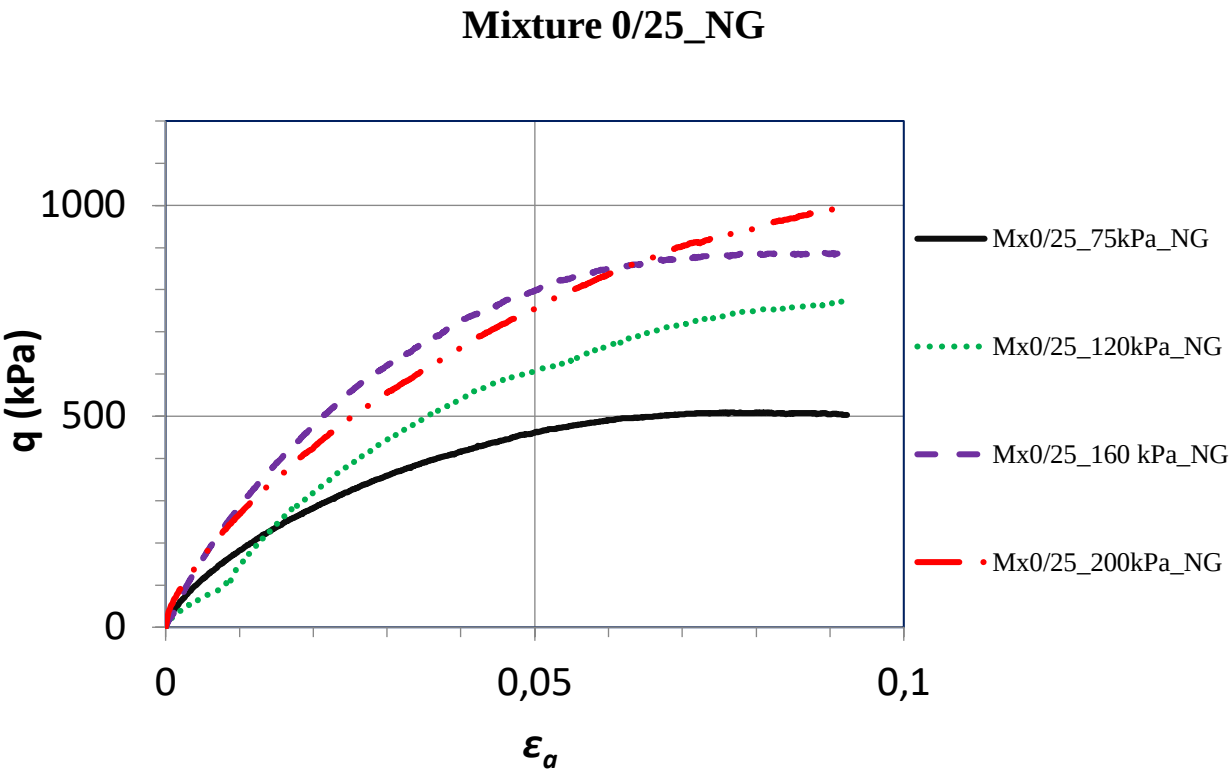

Figure 34. q v. ε_a plot for Mixture 0/25_NG.

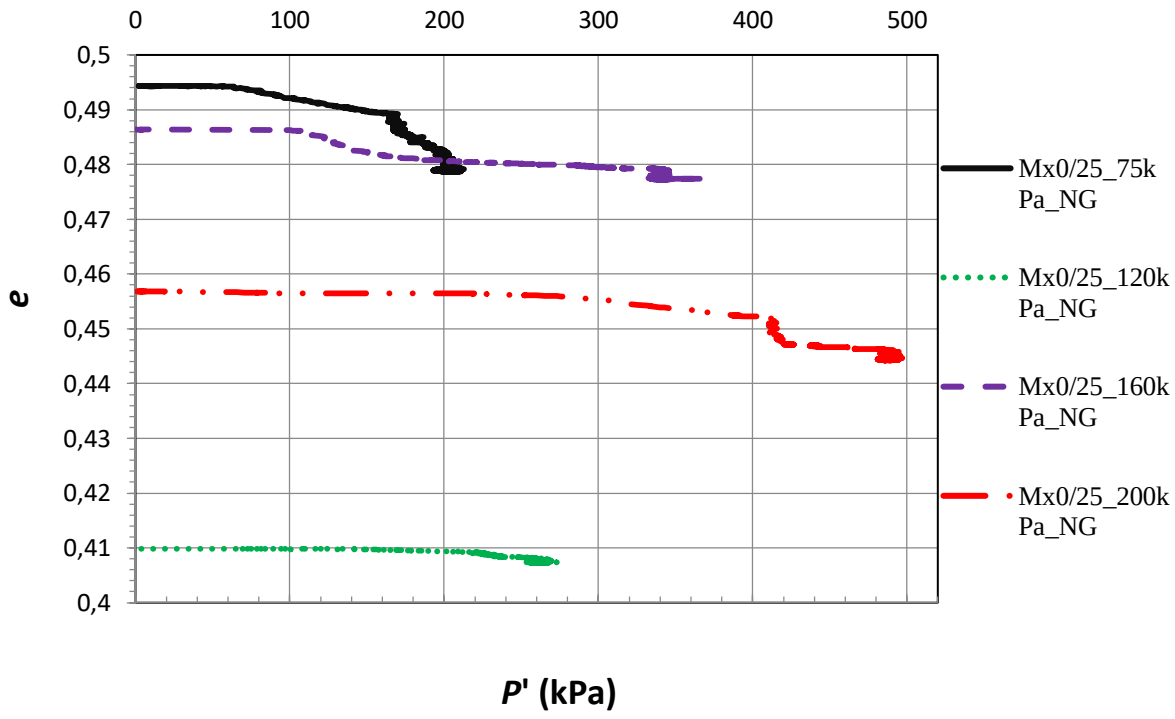

Figure 35. e v. p' plot for Mixture 0/25_NG.

During shearing the material response was ductile, showing a relatively smooth build-up to the strength limit. The response was initially contractive, followed by some small dilatancy, generally at larger strains (Figure 36). The exception was test Mx0/25_120kPa_NG, where dilatancy occurred without previous compression, which could be a result of poor contact of the lateral transducers. The strength envelope (Figure 37) for these tests indicate that M = 1.97 or else φ' = 47.8º.

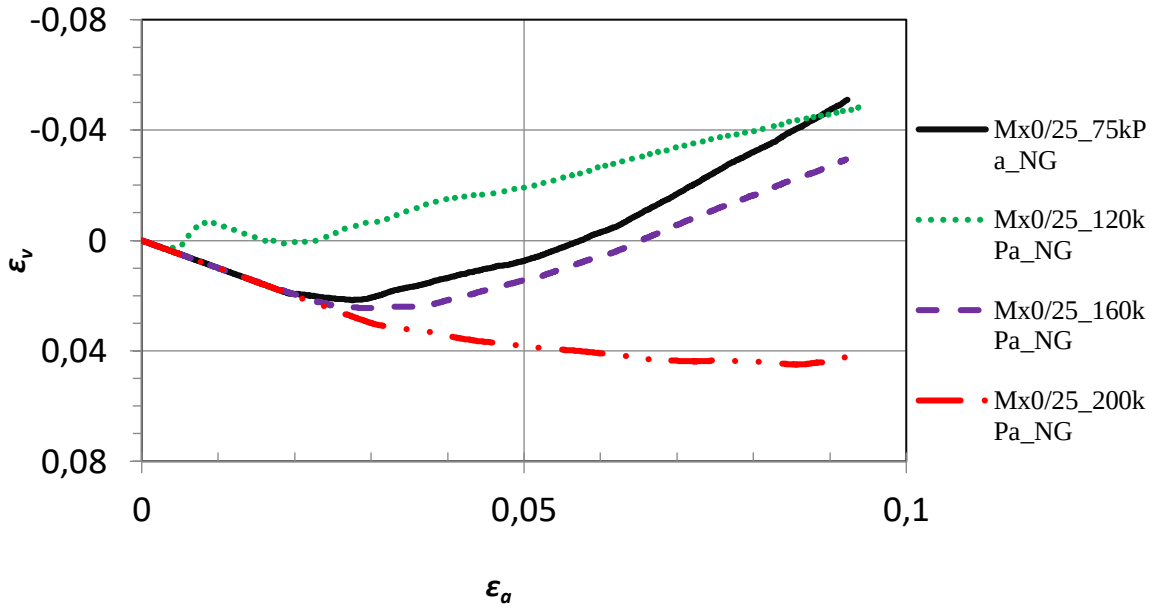

Figure 36. ε_a v. ε_v plot for Mixture 0/25_NG.

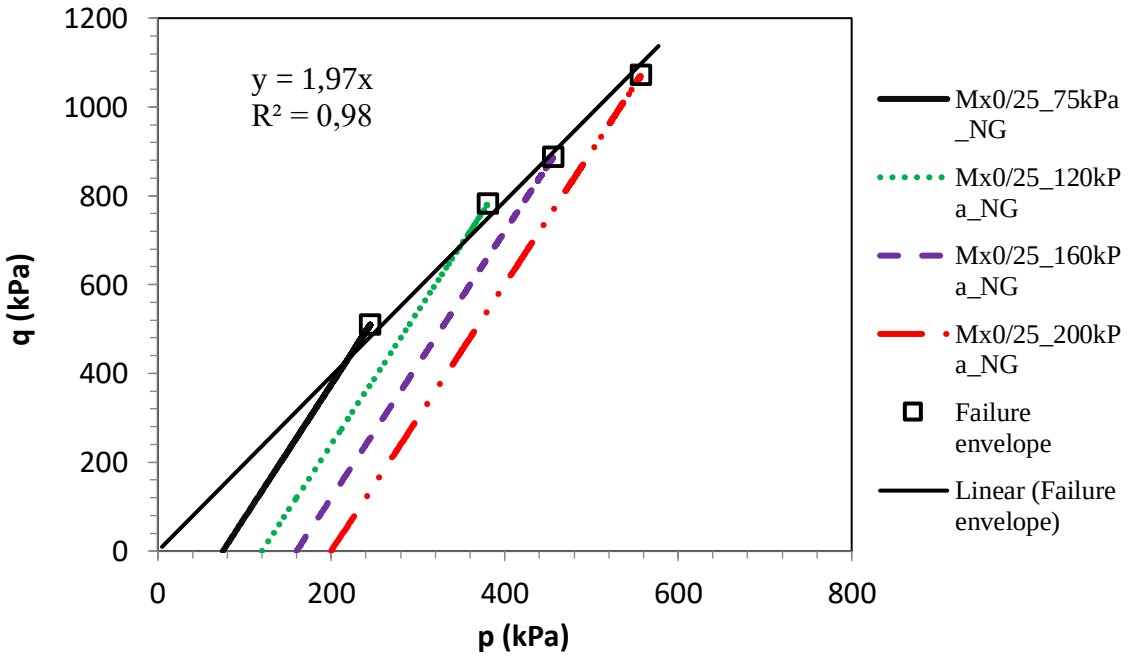

Figure 37. Strength envelope in the Cambridge plane for Mixture 0/25_NG.

7.2.2. Mx0/25_Tx150

Results from the test series with geogrid Tx150 on the Mixture 0/25 are presented in figures Figure 38 to Figure 41. For the tests with reinforced layer by geogrids it was expected to obtain higher deviatoric stress in comparison with results from series without geogrid.

Similar increasing pattern of deviatoric stress was observed for all test. However, compaction of the sample Mx0/25_200kPa_Tx150 during the compression phase was smaller than the compaction of the sample Mx0/25_160kPa_Tx150 (Figure 39), that leads to the decreased values of the deviatoric stress in sample Mx0/25_200kPa_Tx150 (Figure 38).

In Figure 40 represented that response was generally contractive, although some samples showed some dilatancy in advanced shearing stages. The strength envelope showed increased parameters which became equal to M = 2.08 and φ' = 50.5º.

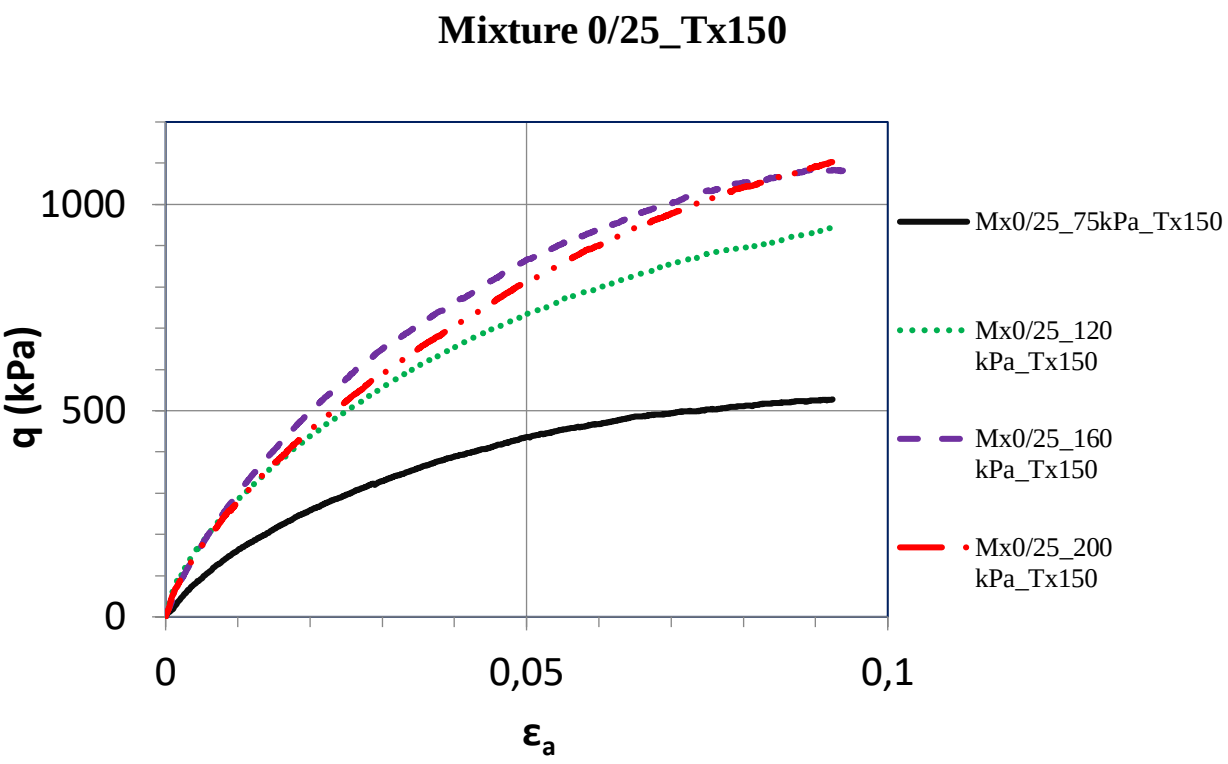

Figure 38. q v. ε_a plot for Mixture 0/25_Tx150.

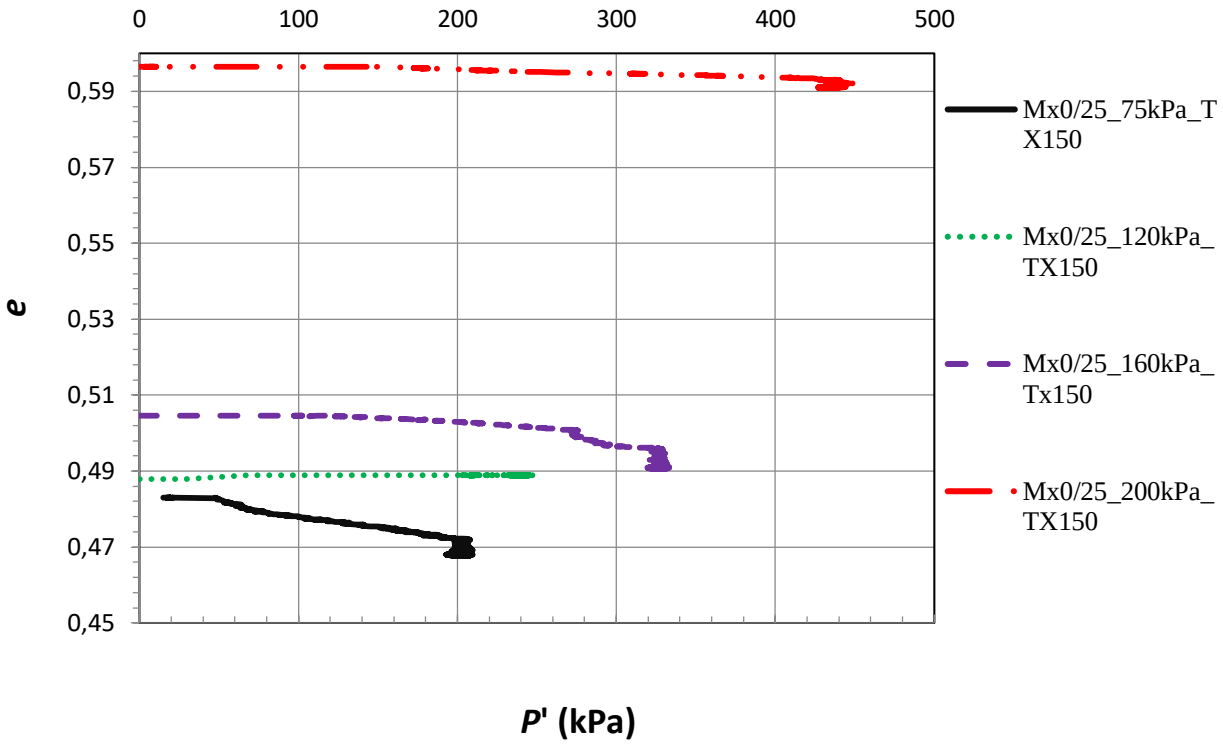

Figure 39. *e* v. *p'* plot for Mixture 0/25_Tx150.

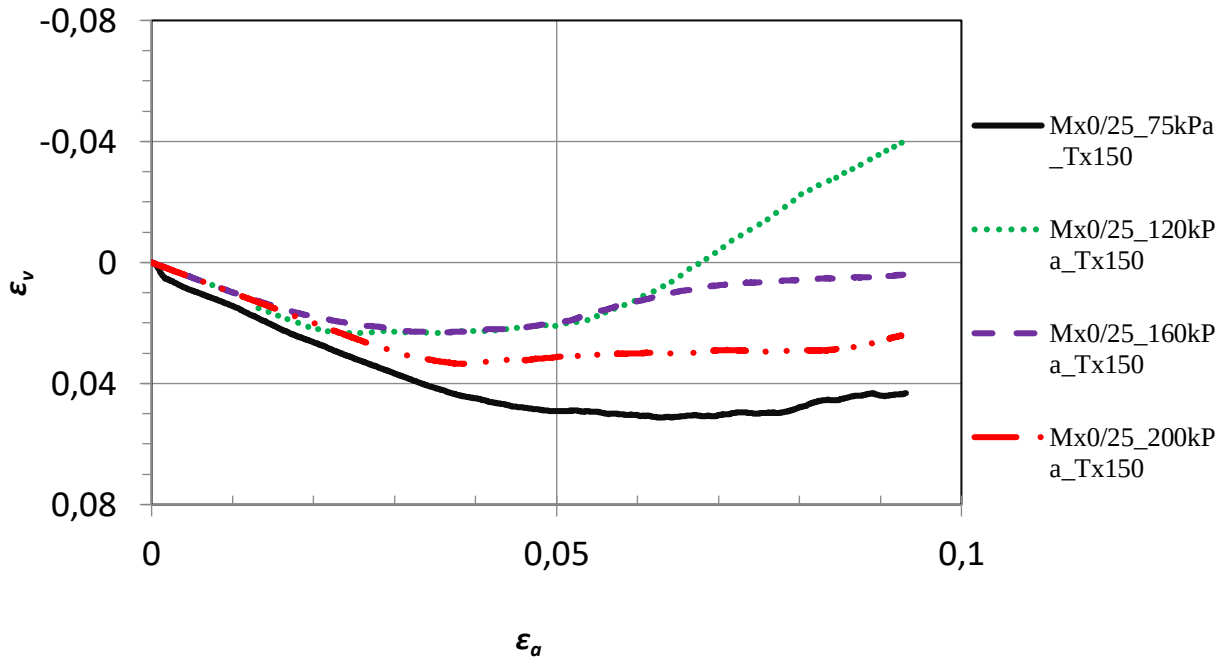

Figure 40. ε_a v. ε_v plot for Mixture 0/25_Tx150.

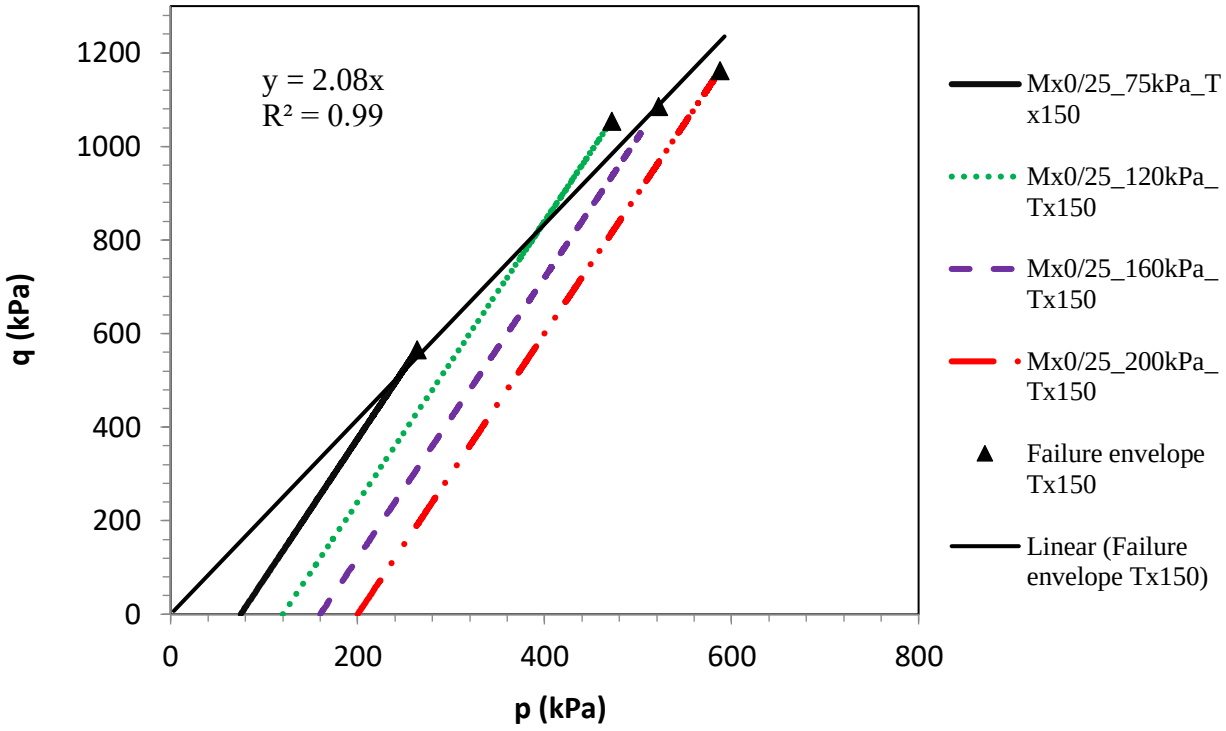

Figure 41. Strength envelope in the Cambridge plane for Mixture 0/25_Tx150.

7.2.3. Mx0/25_Tx170

As it was mentioned in section 4.2.2 starting with the test series Mx0/25_Tx170 compaction procedure during sample preparation has been changed. Stabilized initial void ratios are represented in Figure 43. This made a compaction during the isotropic compression phase became approximately equal for all tests.

During the shear phase the material response was ductile, showing a relatively smooth build-up to the strength limit (Figure 42).

Contractive response with lately dilatancy were observed for all specimens in Figure 39. Obtained slope on strength envelope plot (Figure 45) was equal to M = 2.08 and φ' = 50.5º.

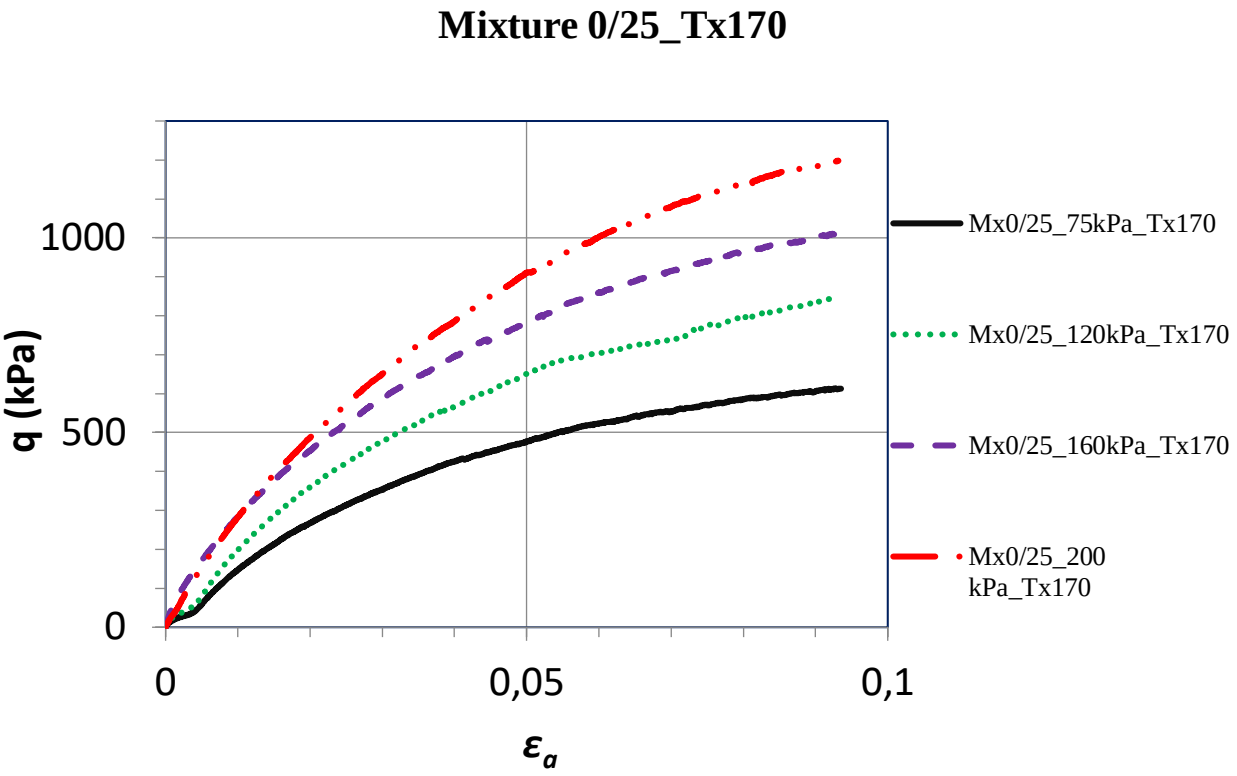

Figure 42. q v. ε_a plot for Mixture 0/25_Tx170.

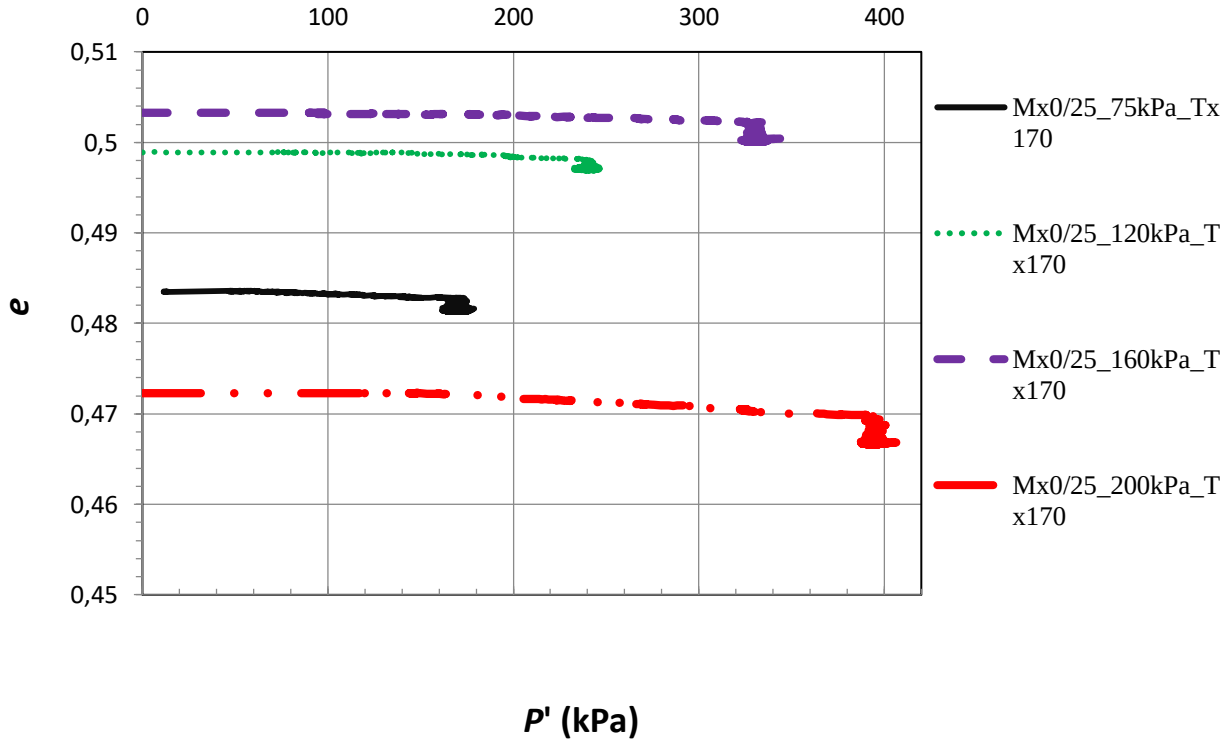

Figure 43. e v. p' plot for Mixture 0/25_Tx170.

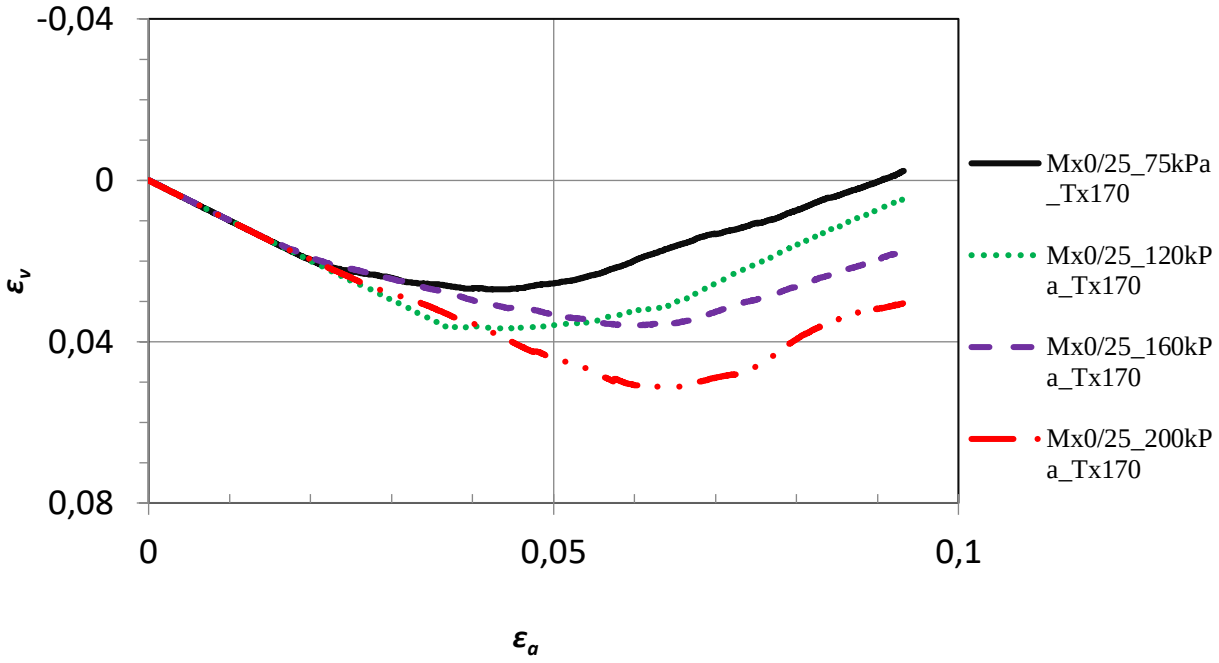

Figure 44. ε_a v. ε_v plot for Mixture 0/25_Tx170.

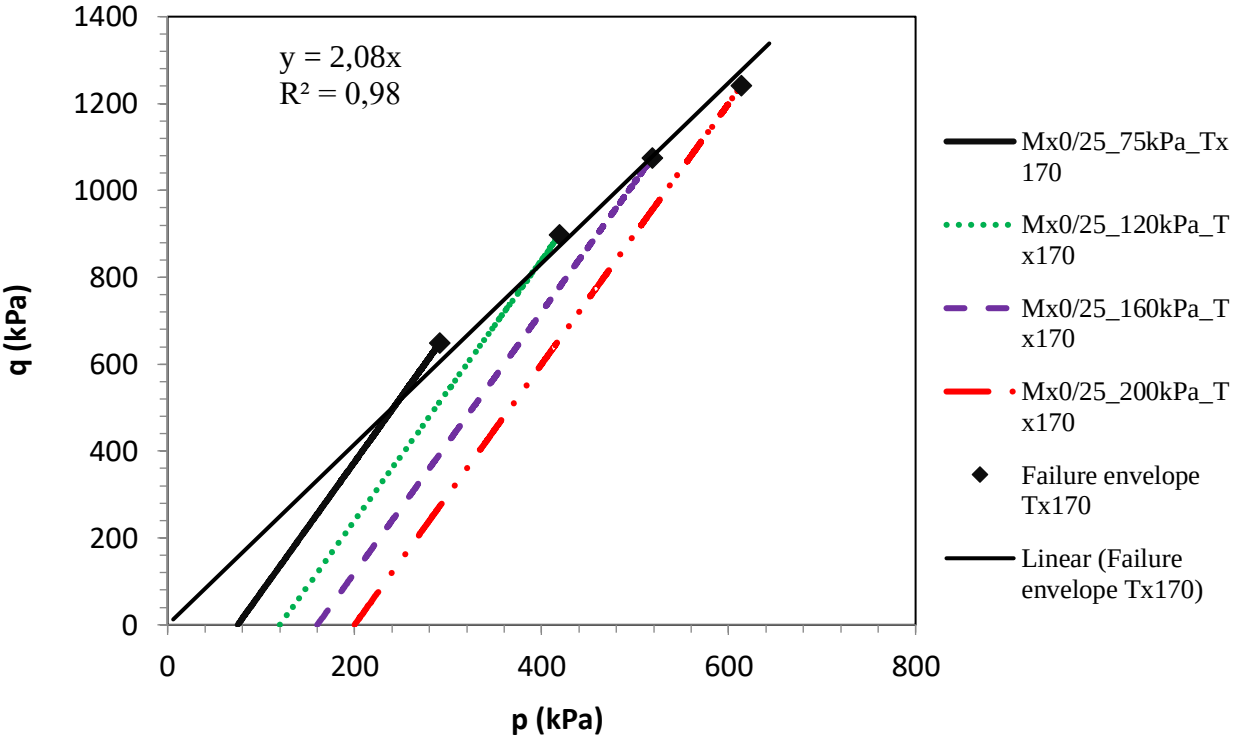

Figure 45. Strength envelope in the Cambridge plane for Mixture 0/25_Tx170.

7.2.4. Mx10/25_NG

Test series on new material “Mixture 10/25” were accomplished by same procedure except that the materials were sieved before and after each test. Pressure applied during isotropic compression phase has compacted specimen as shown in Figure 47.

During the shear phase it was observed that specimen Mx10/25_75kPa_NG has almost reached a peak strength at 7% of axial strain (Figure 46). Moreover, it was noticed that all samples had a contraction in the beginning of share phase and dilatancy effect in lately stages of shearing, except test Mx10/25_160kPa_NG (Figure 48). One of the possible problems for such behavior has been found as a deformation of the internal rod and incorrect readings of the LVDT’s. The strength envelope indicates that M = 1.80 or else φ’ = 44º.

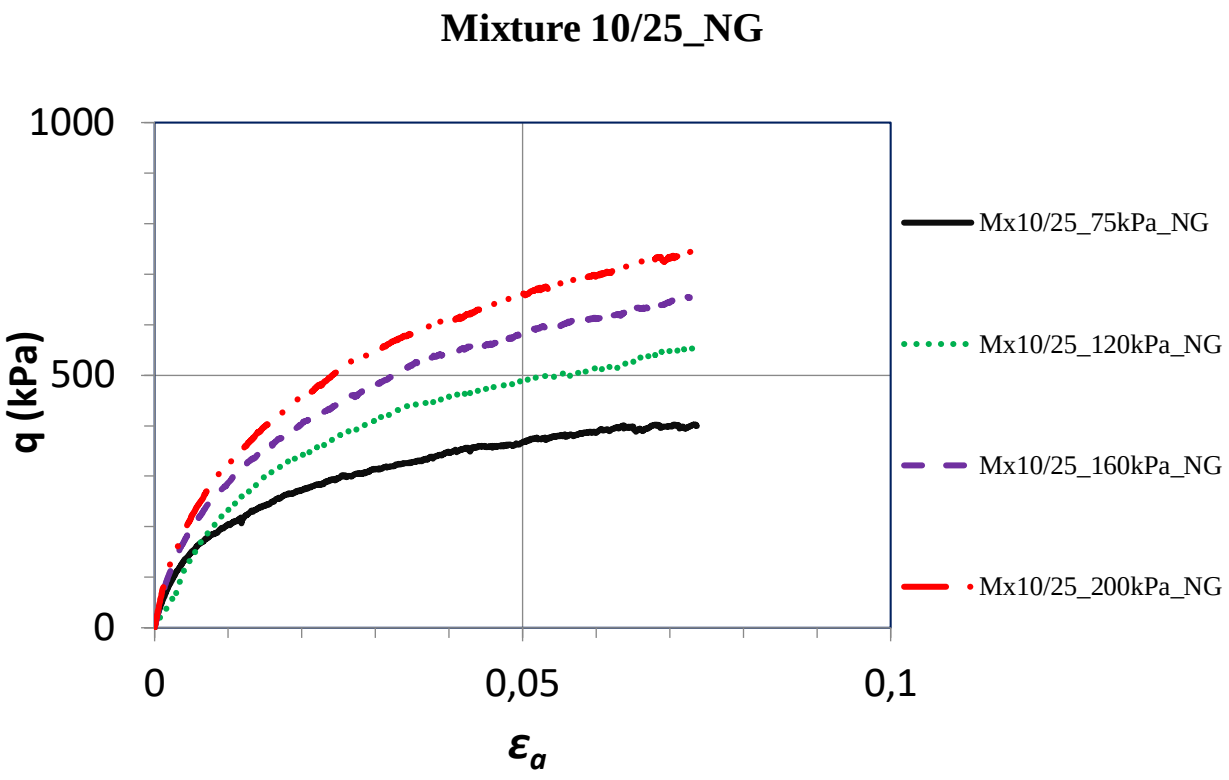

Figure 46. q v. ε_a plot for Mixture 10/25_NG.

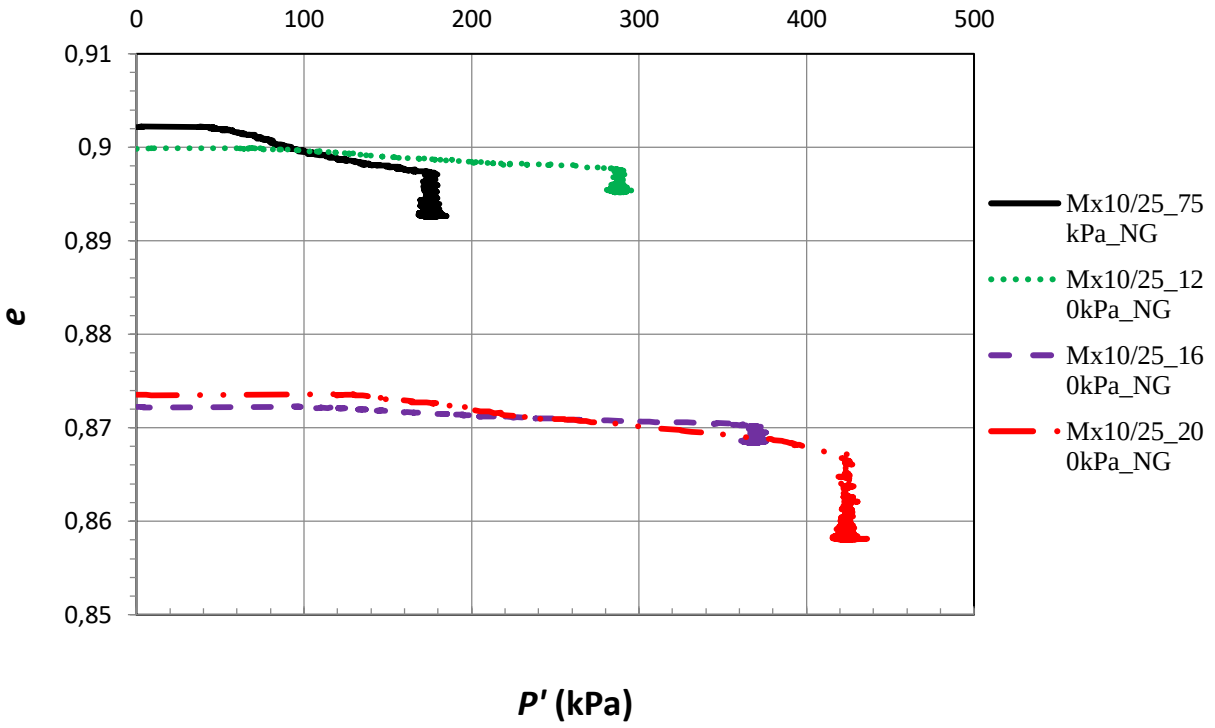

Figure 47. *e* v. *p'* plot for Mixture 10/25_NG.

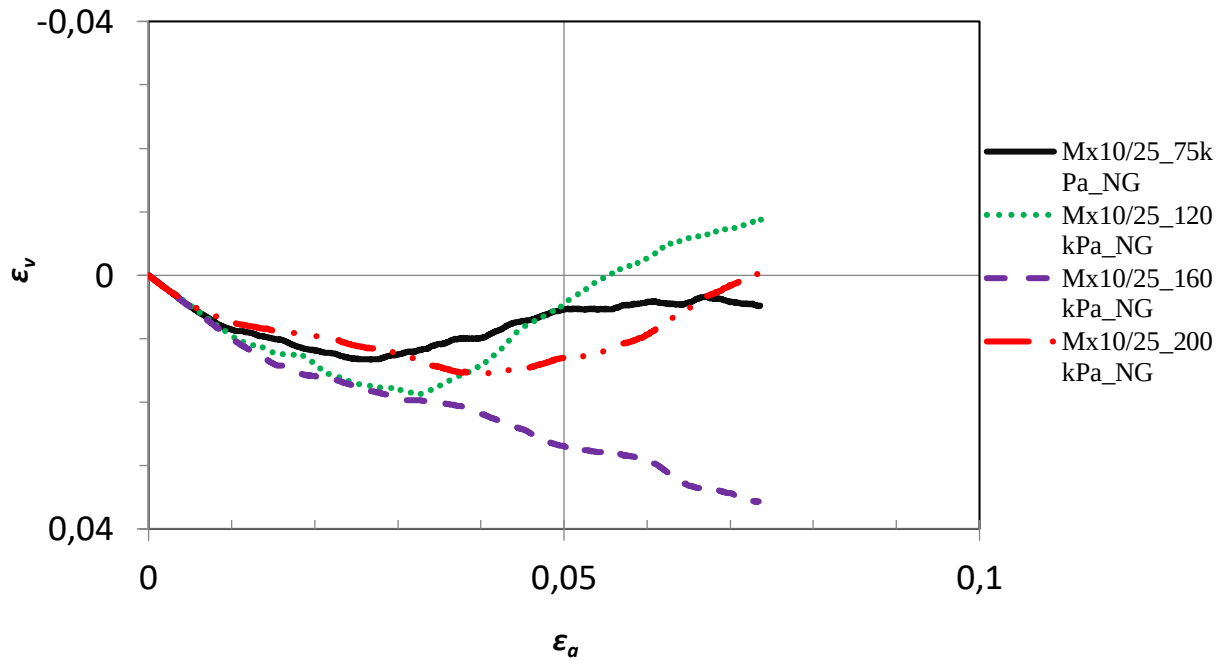

Figure 48. ε_a v. ε_v plot for Mixture 10/25_NG.

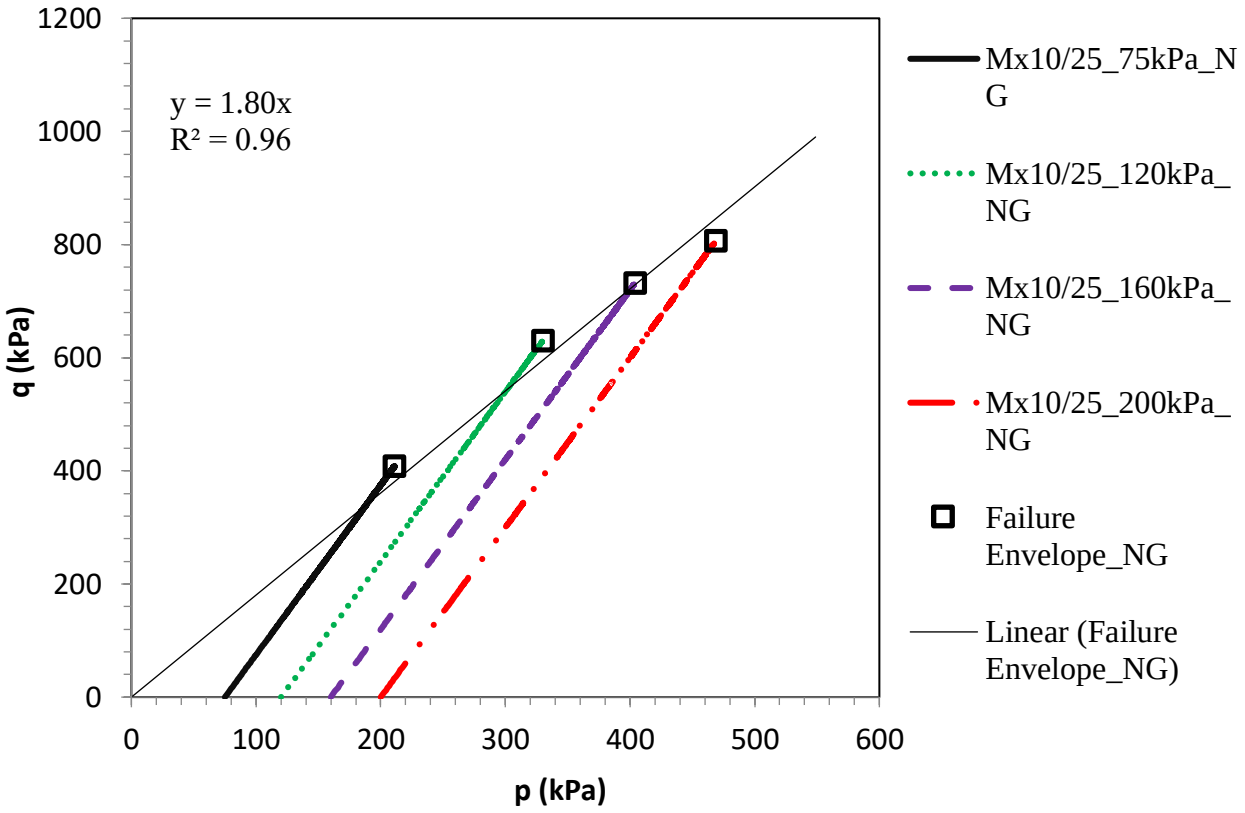

Figure 49. Strength envelope in the Cambridge plane for Mixture 10/25_NG.

7.2.5. Mx10/25_Tx150

For test series Mx10/25_Tx150 results are presented in figures Figure 50 to Figure 53. A small compaction of all materials was observed during isotropic compression phase (Figure 51), leading to the ductile response during shear phase and smooth build-up of the strength limit (Figure 50).

Volumetric deformation, which is shown in Figure 52, indicated that samples had a contraction in the beginning of shearing phase and dilatancy during the latter stages. Exception is observed in sample Mx10/25_200kPa_Tx150 which was subjected to contraction only. Again, occurred problem could be related to one of the problems discussed in Section 5.3.

Strength envelope was built for reinforced sample and calculated M = 1.88 or else φ' = 46º.

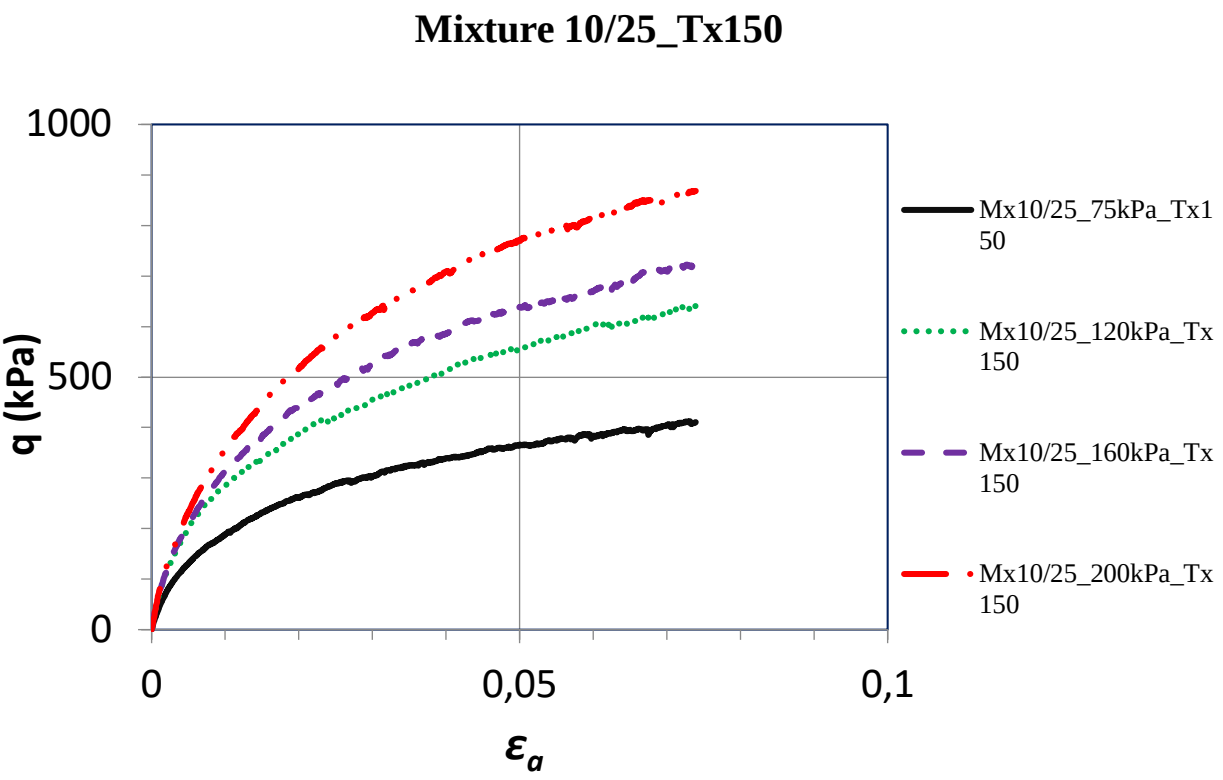

Figure 50. q v. ε_a plot for Mixture 10/25_Tx150.

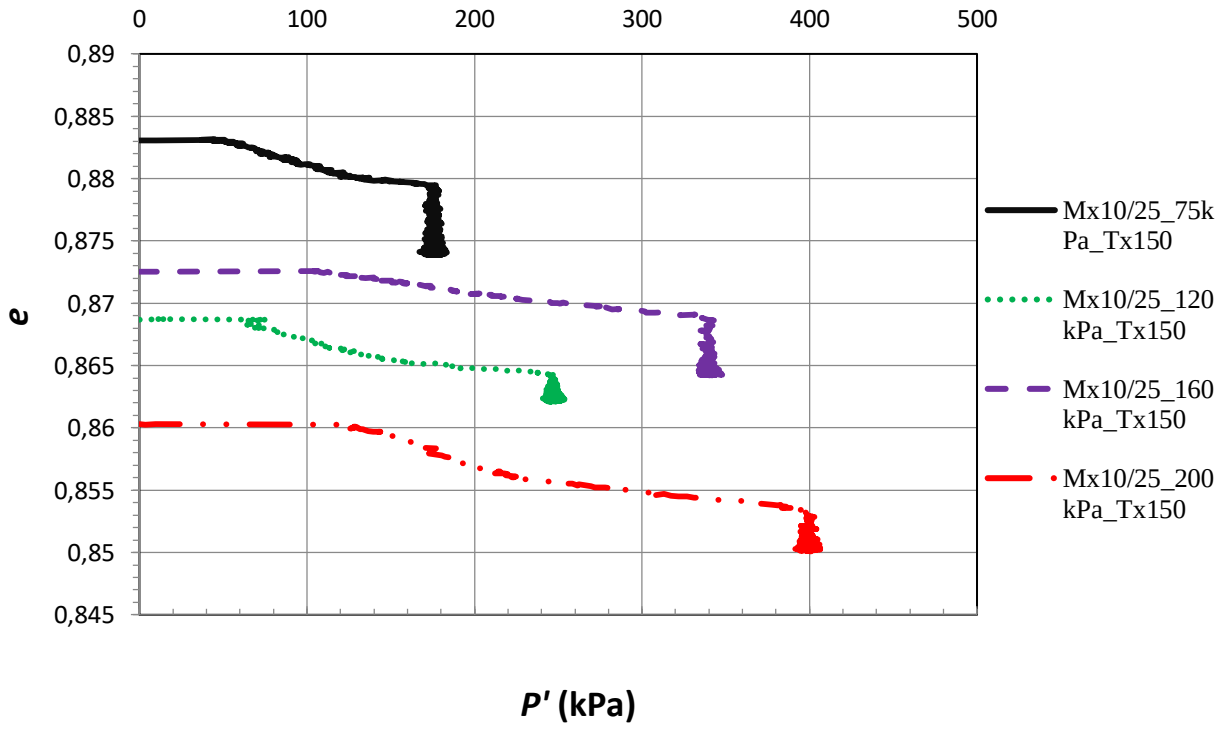

Figure 51. e v. p' plot for Mixture 10/25_Tx150.

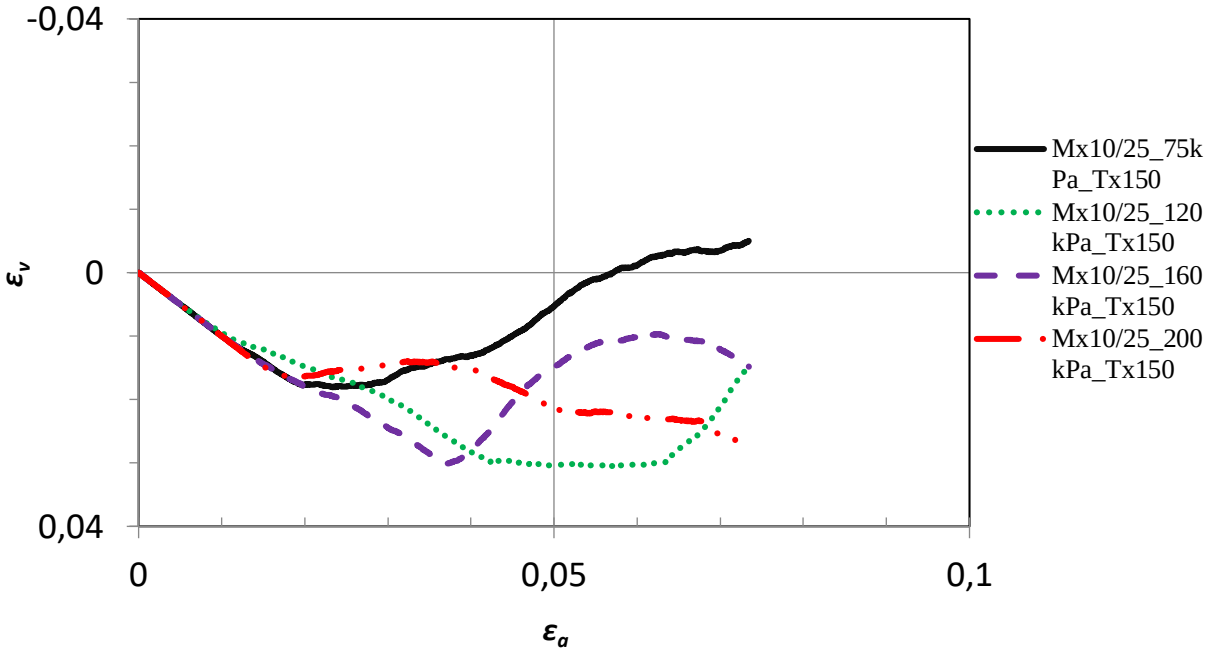

Figure 52. ε_a v. ε_v plot for Mixture 10/25_Tx150.

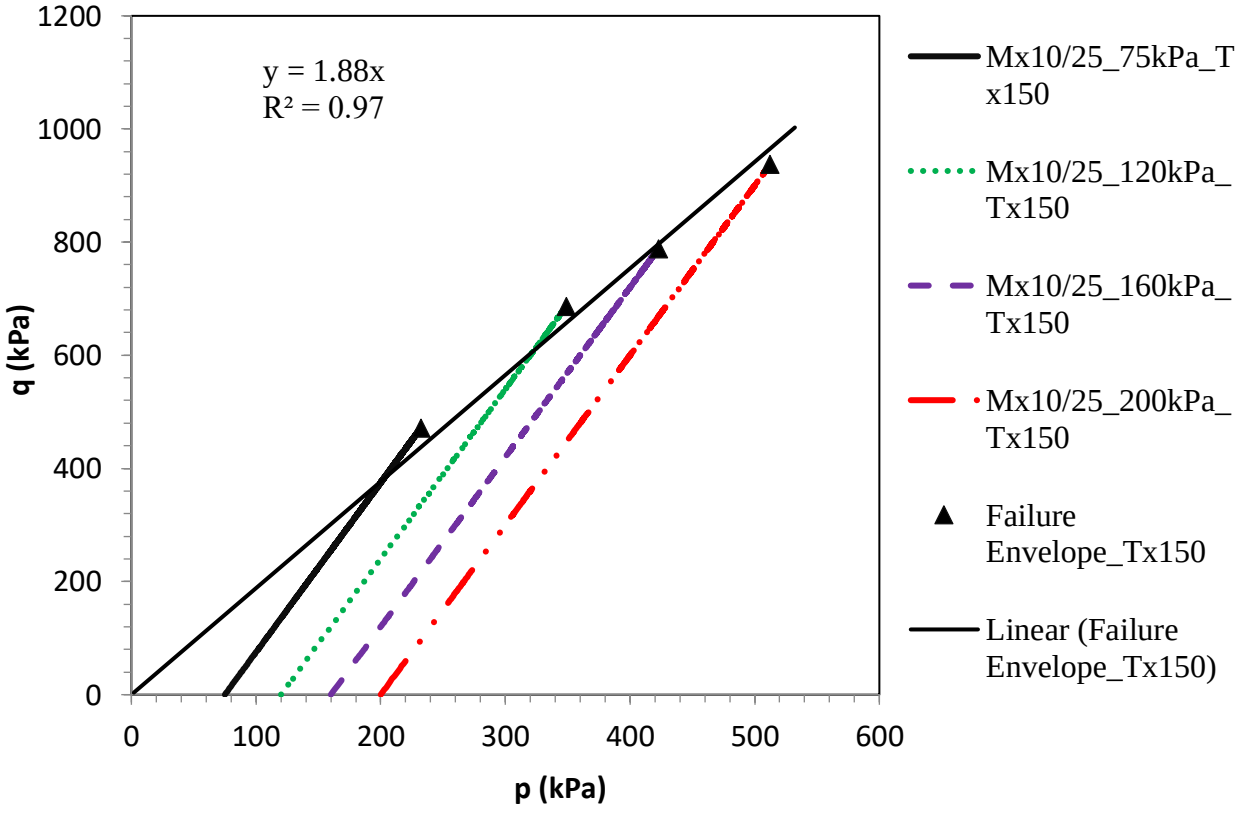

Figure 53. Strength envelope in the Cambridge plane for Mixture 10/25_Tx150.

7.2.6. Mx10/25_Tx170

In figures Figure 54 to Figure 57 results for samples, reinforced by geogrid Tx170, are represented. Relatively high compaction (Figure 55) during the isotropic compression phase can be observed in sample Mx10/25_200kPa_Tx170. Nevertheless, effect of the compaction during isotropic compression phase was not noticed in the plot of deviatoric stress (Figure 54), as it was detected in Mx0/25 samples, where poor compaction was leading to the reduced strength.

It was inspected that only sample Mx10/25_75kPa_Tx170 had a dilatancy effect, while other samples were subjected to the contraction only. Calculated slope for strength envelope was M = 1.87 or φ' = 45.5º.

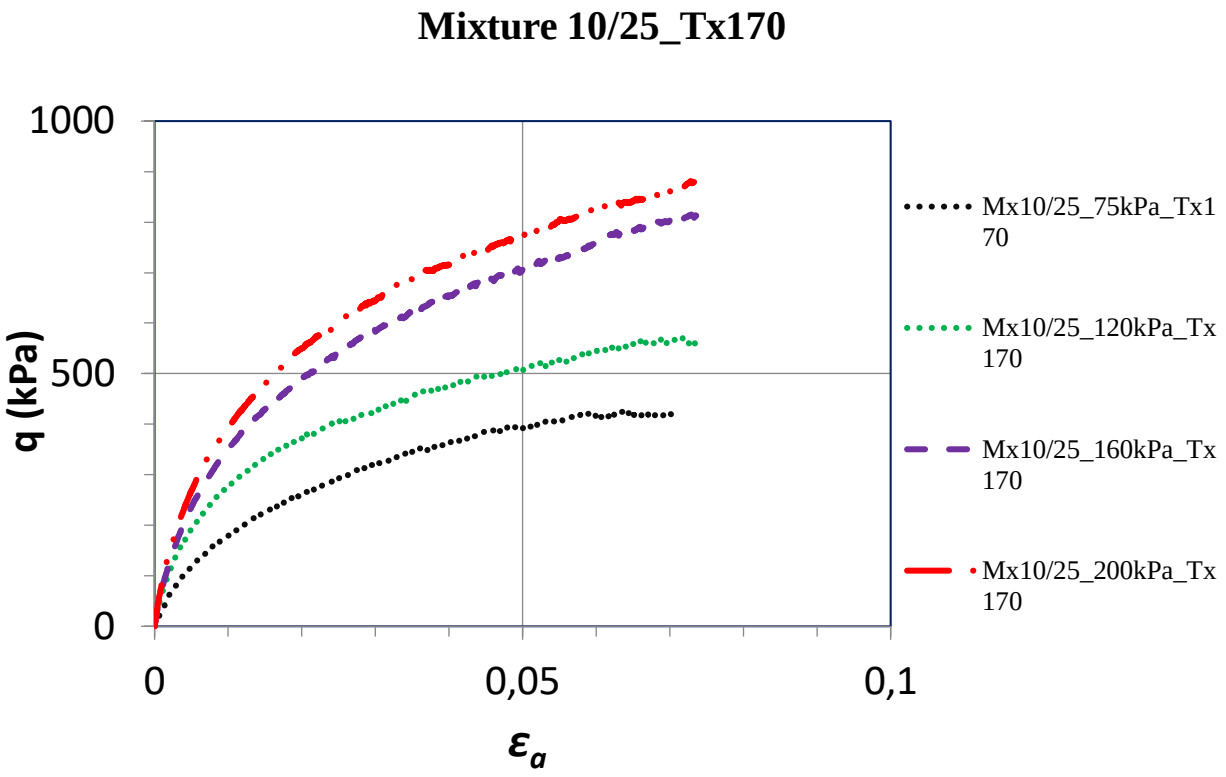

Figure 54. q v. ε_a plot for Mixture 10/25_Tx170.

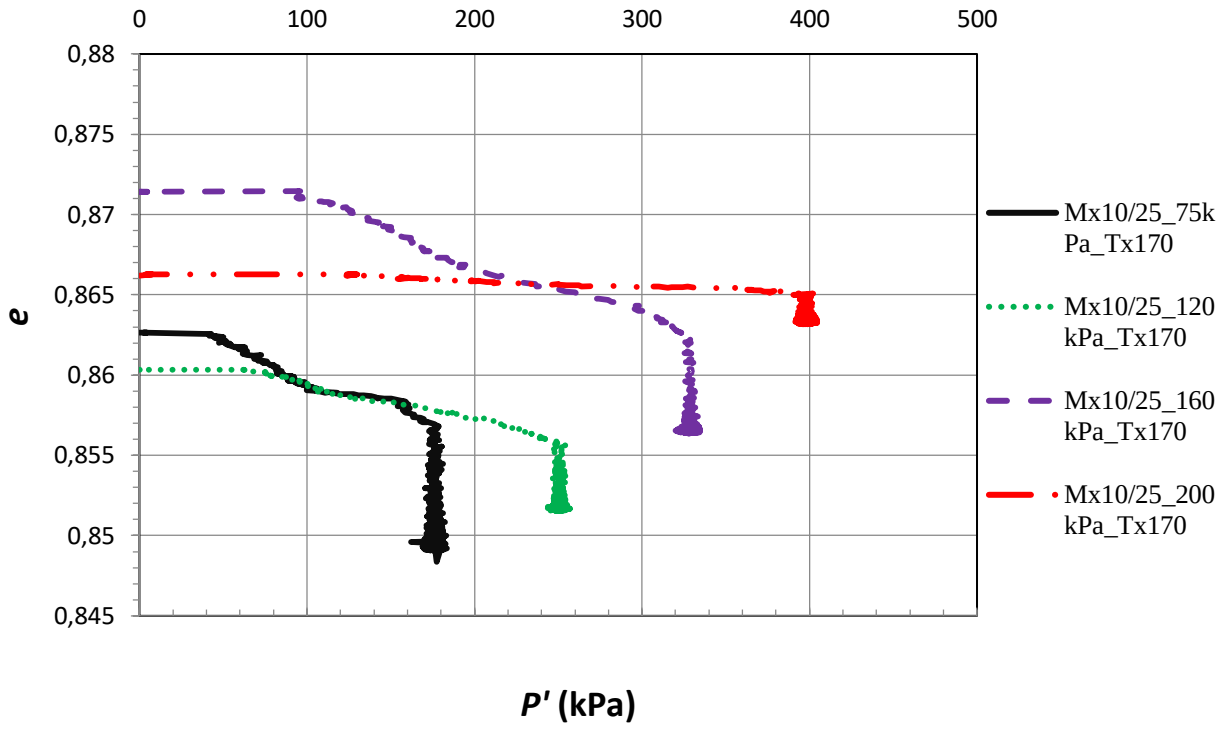

Figure 55. *e* v. *p'* plot for Mixture 10/25_Tx170.

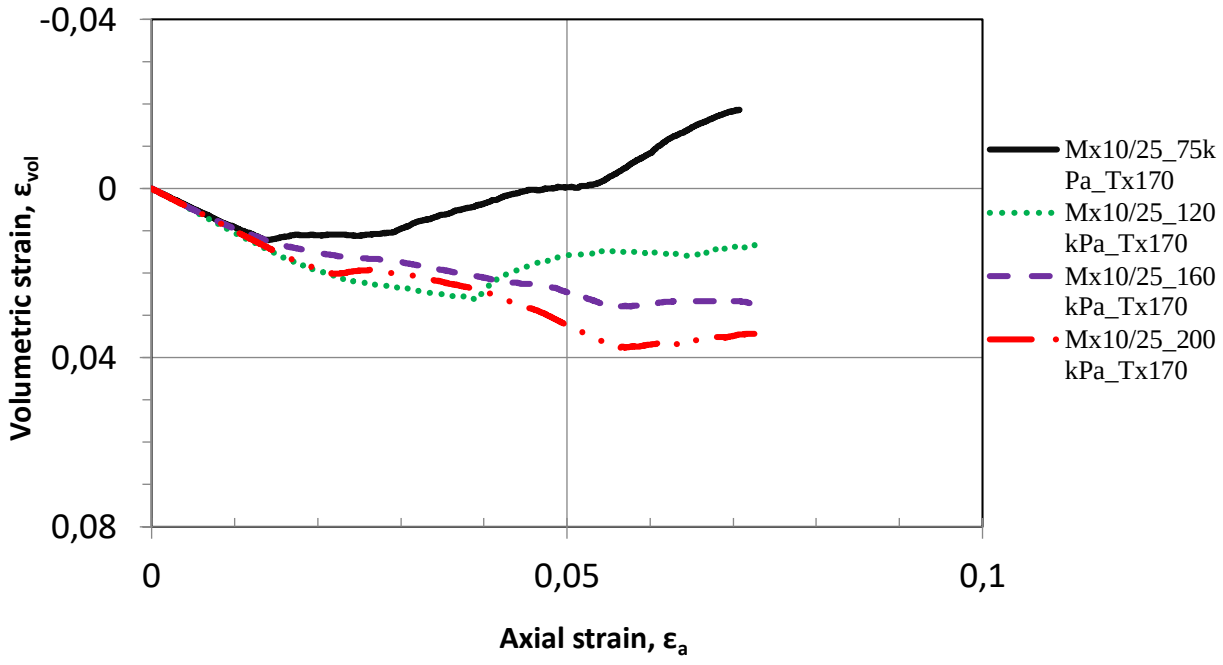

Figure 56. ε_a v. ε_v plot for Mixture 10/25_Tx170.

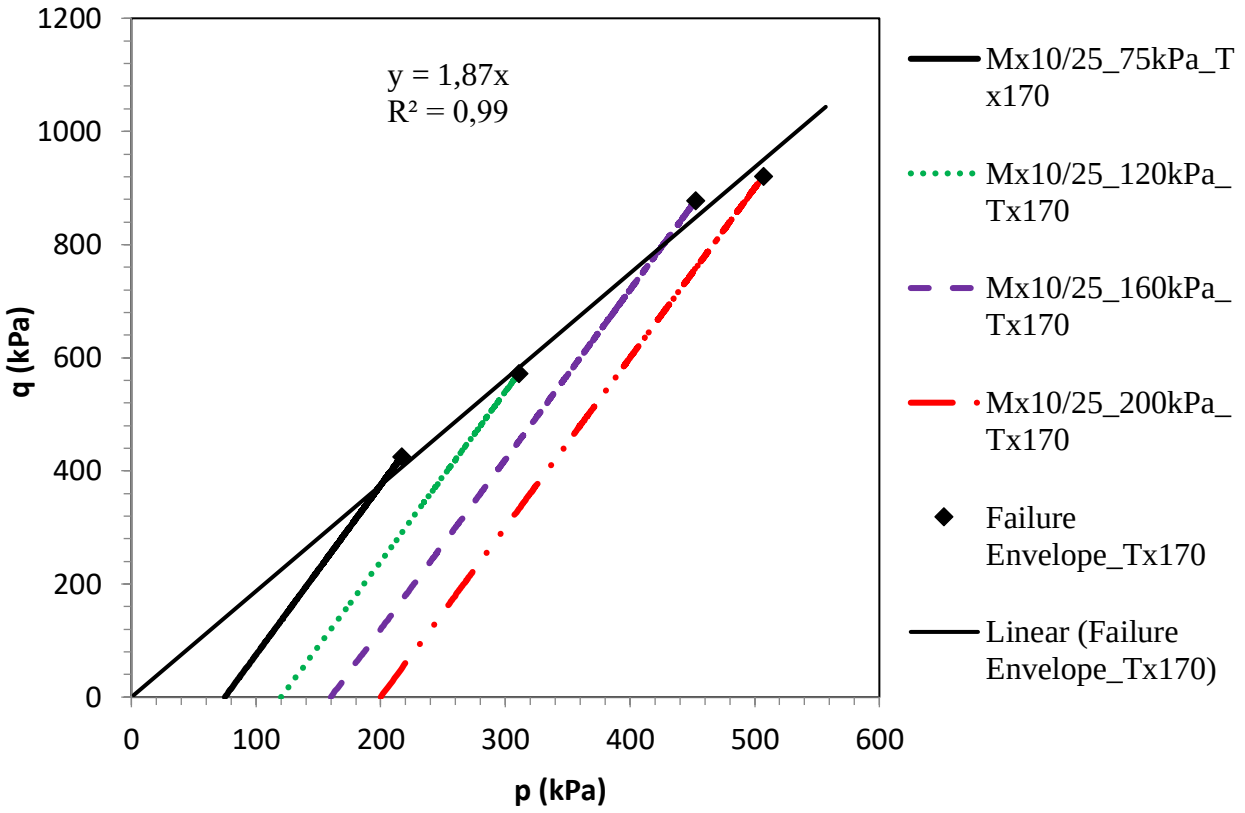

Figure 57. Strength envelope in the Cambridge plane for Mixture 10/25_Tx170.

8. Comparison and discussion

8.1. Comparison of Mx0/25

Comparison between non-reinforced and reinforced material, by different geogrids, are presented in this section. In Figure 58 the strength envelopes obtained for the Mixture 0/25 material with and without geogrid reinforcement are compared. There is a significant difference in the envelopes between reinforced and non-reinforced samples, however samples which were reinforced by different geogrids showed similar failure envelopes, as summarized in Table 6. The reinforced specimen is found to be stronger than non-reinforced one, but the strength difference is not observed for samples which were reinforced by different geogrid. The presence of the geogrid results in a friction angle increase up to 50.5.

In Figure 59 plot of deviatoric stress against axial strain for Mixture 0/25 at 120kPa confining pressure is presented. As it can be seen the strength of the sample which was reinforced by geogrid Tx150 is higher in comparison with the results for sample reinforced by geogrid Tx170. Similar behavior is noticed for the Mx0/25_160kPa samples (Figure 60). Such response could be a result

of the problems that occurred during test and discussed in Section 5.3. While for the tests at 75kPa and 200 kPa confining pressures (Figure 61 and Figure 62 respectively), it was observed a rise of the strength with the increasing stabilization of the specimen.

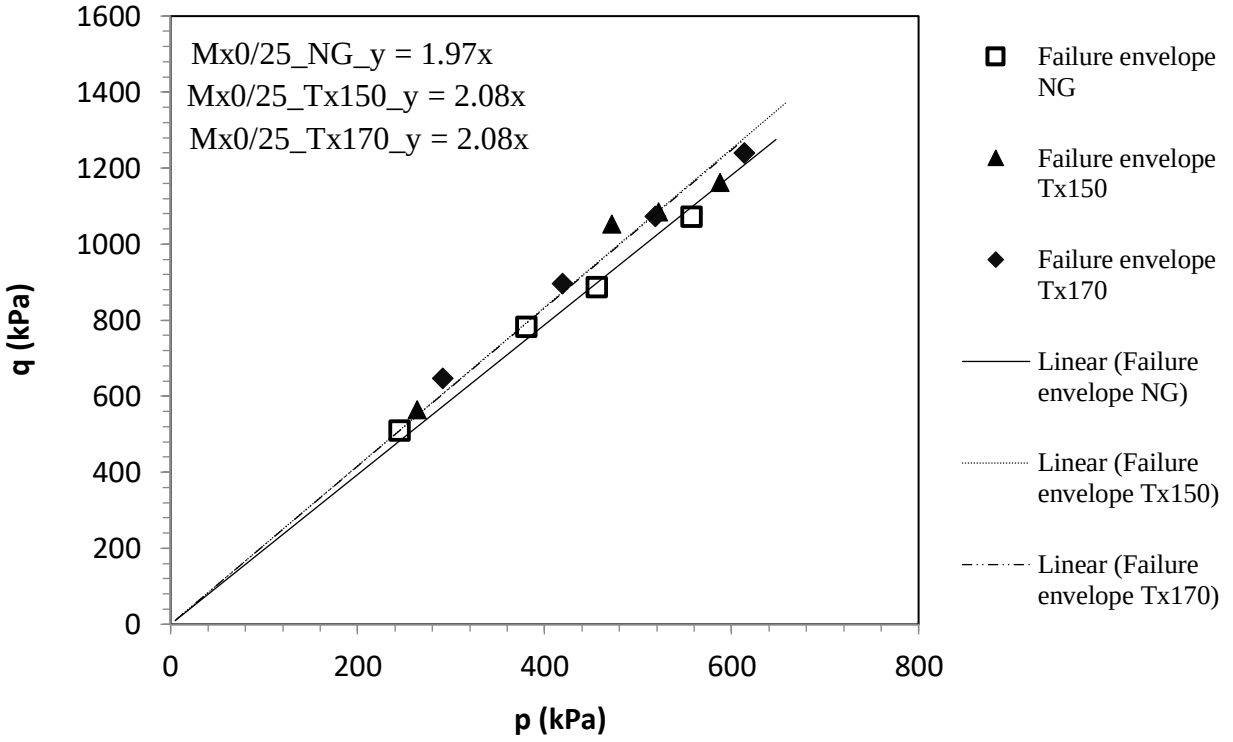

Figure 58. Failure envelopes for Mixture 0/25.

Table 6. Strength envelope parameters for Mixture 0/25.

Parameter	NG	Tx150	Tx170
M	1.97	2.08	2.08
φ’	47.8^{o}	50.5^{o}	50.5^{o}

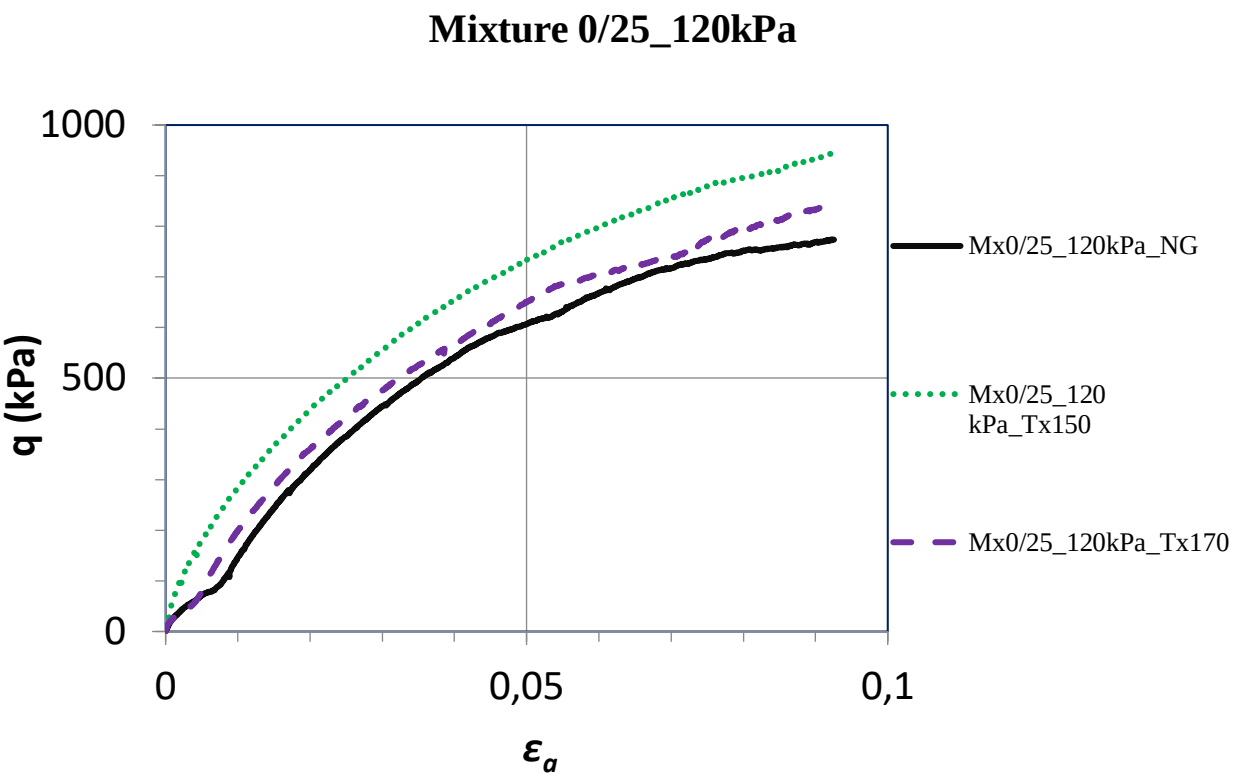

Figure 59. q v. ε_a plot for Mixture 0/25_120kPa.

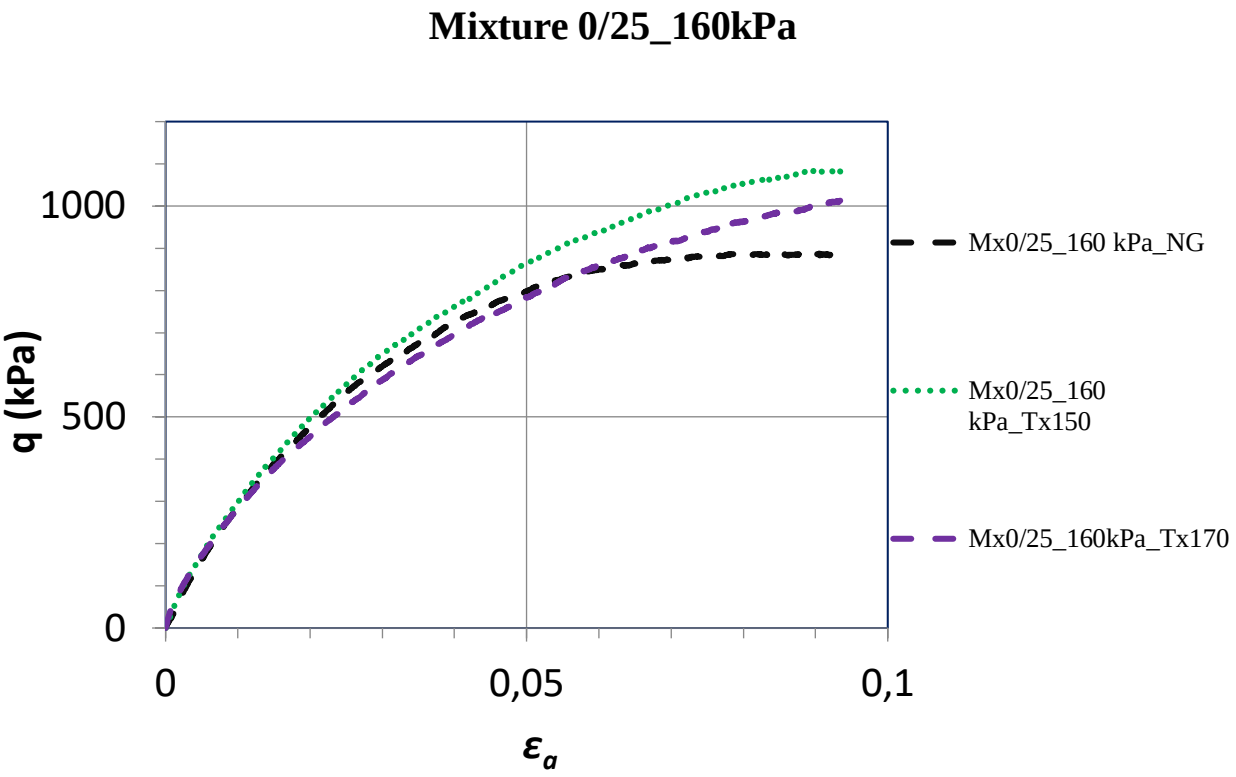

Figure 60. q v. ε_a plot for Mixture 0/25_160kPa.

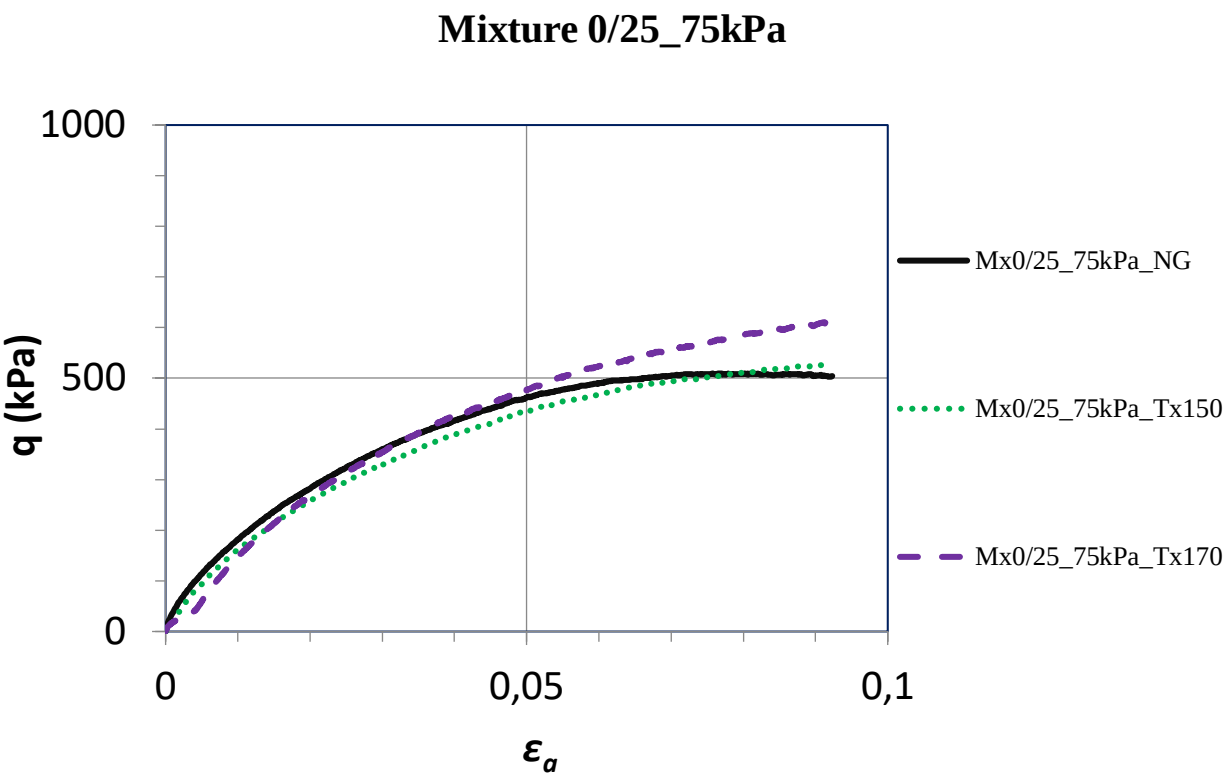

Figure 61. q v. ε_a plot for Mixture 0/25_75kPa.

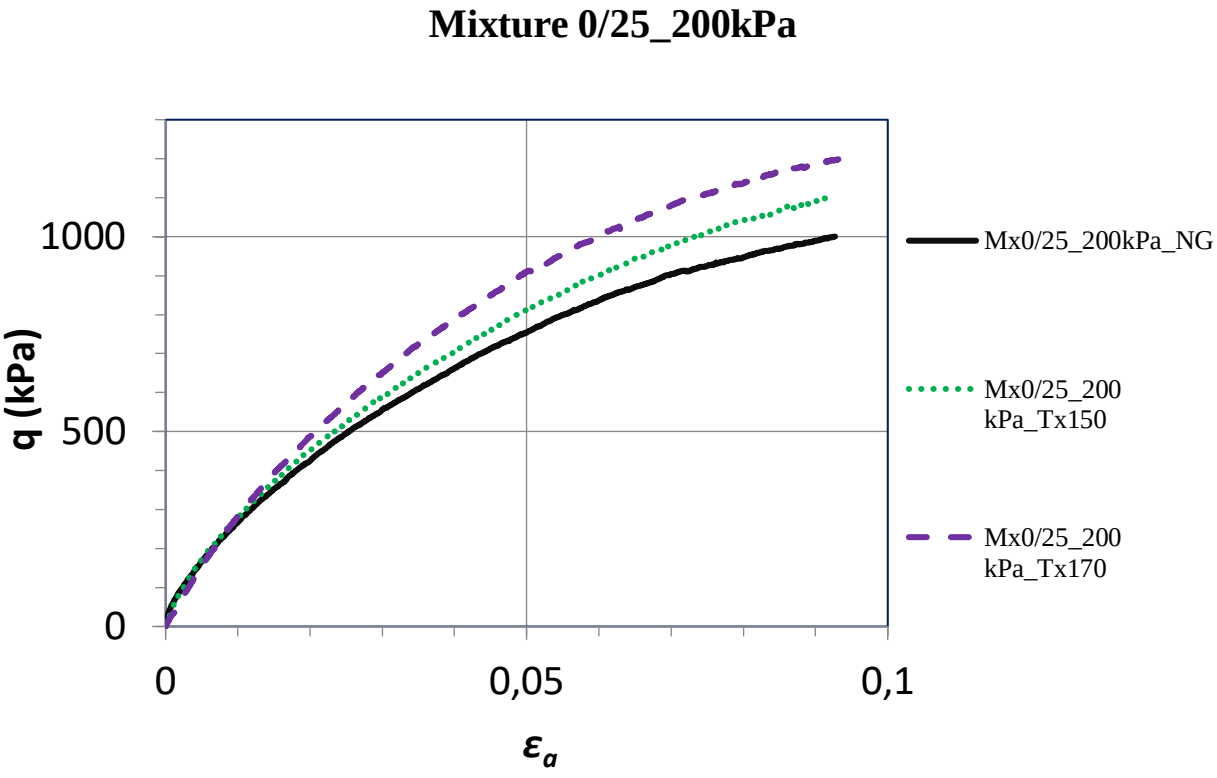

Figure 62. q v. ε_a plot for Mixture 0/25_200kPa.

8.2. Comparison of Mx10/25

In Figure 63 the strength envelopes obtained for Mixture 10/25 for all reinforcement conditions are represented. Again the inclusion of geogrids resulted in an increase of strength, but no significant difference between the two geogrids was observed (Table 7).

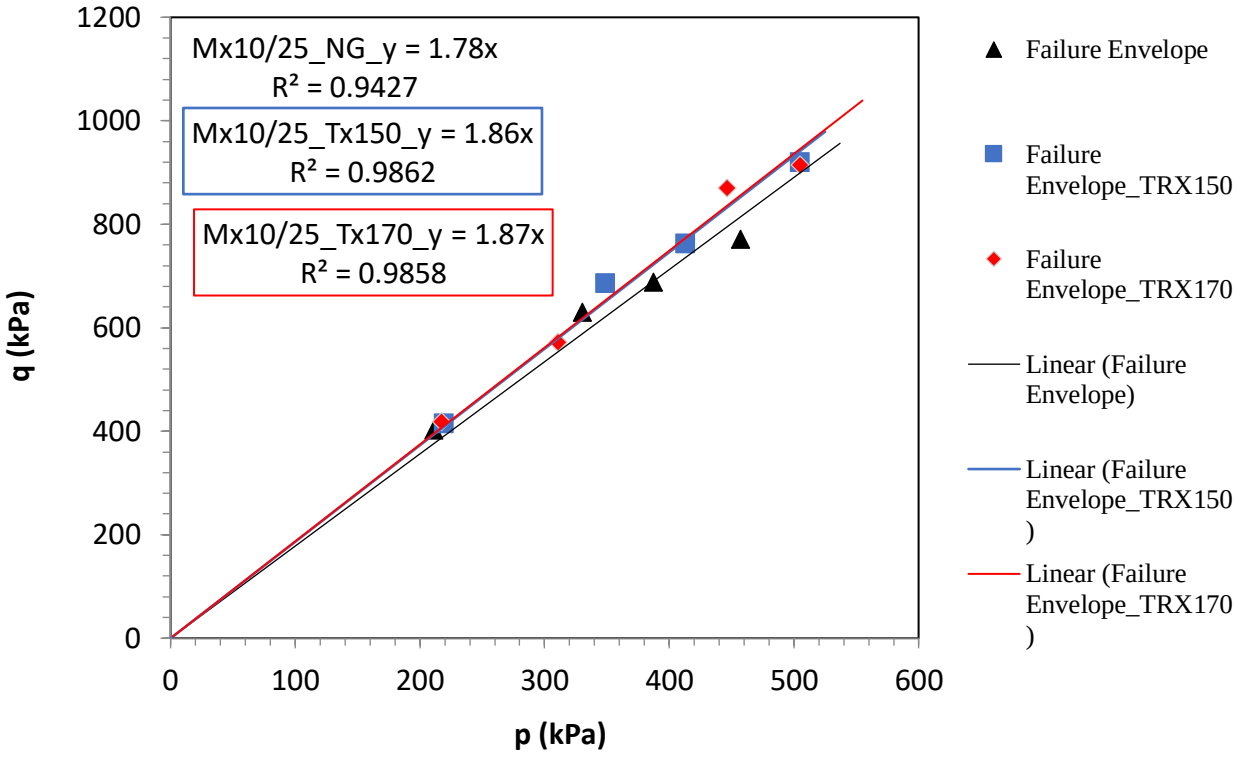

Figure 63. Failure envelopes for Mixture 10/25.

Table 7. Strength envelope parameters for Mixture 10/25.

Parameter	NG	Tx150	Tx170
M	1.78	1.86	1.87
φ’	43.4°	45.3°	45.5°

In figures Figure 64 to Figure 67 graphs of deviatoric stress against axial strain are illustrated. It can be observed that strength of the material at 75kPa pressure was similarl for reinforced Tx150 and non-reinforced conditions. However, at confining pressure of 120kPa strength envelope for geogrid Tx150 was higher than for geogrid Tx170. For sample Mx10/25_200kPa it has been found that deviatoric stress for Tx150 and Tx170 nearly same.

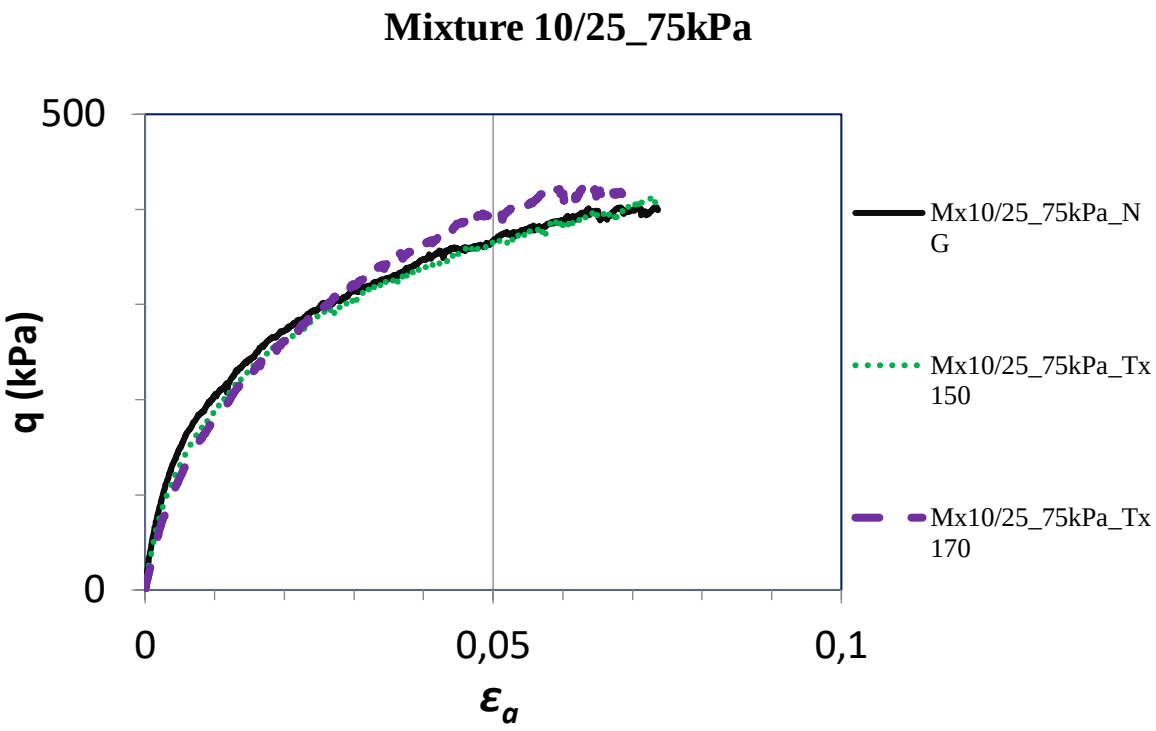

Figure 64. q v. ε_a plot for Mixture 10/25_75kPa.

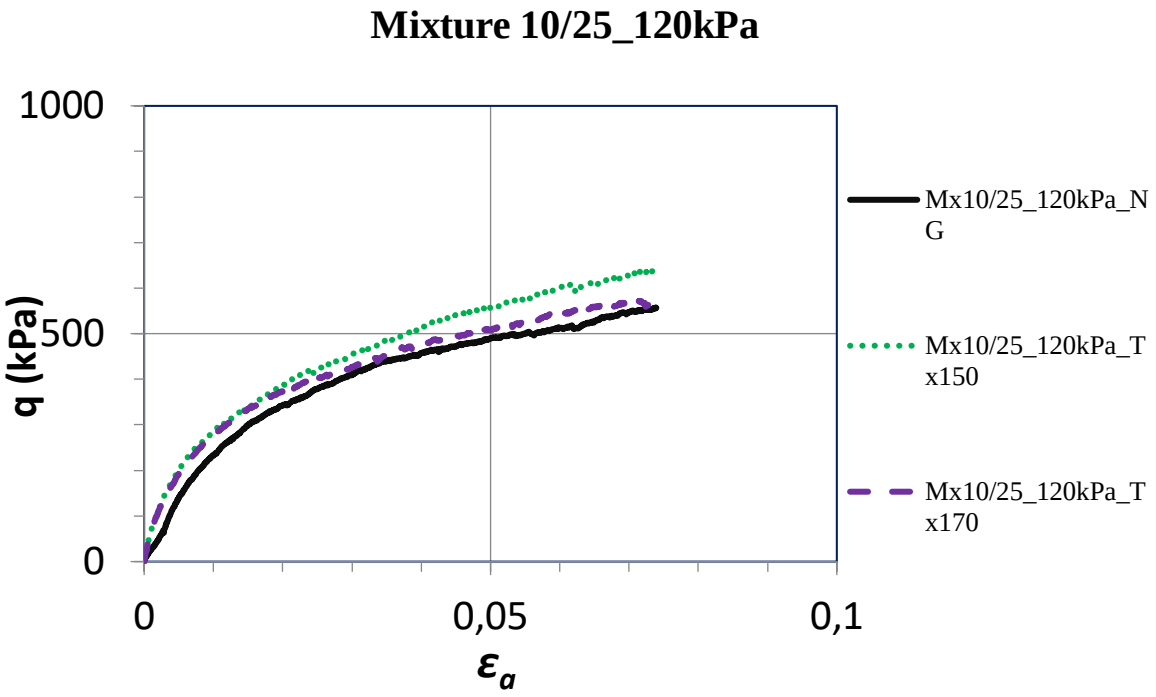

Figure 65. q v. ε_a plot for Mixture 10/25_120kPa.

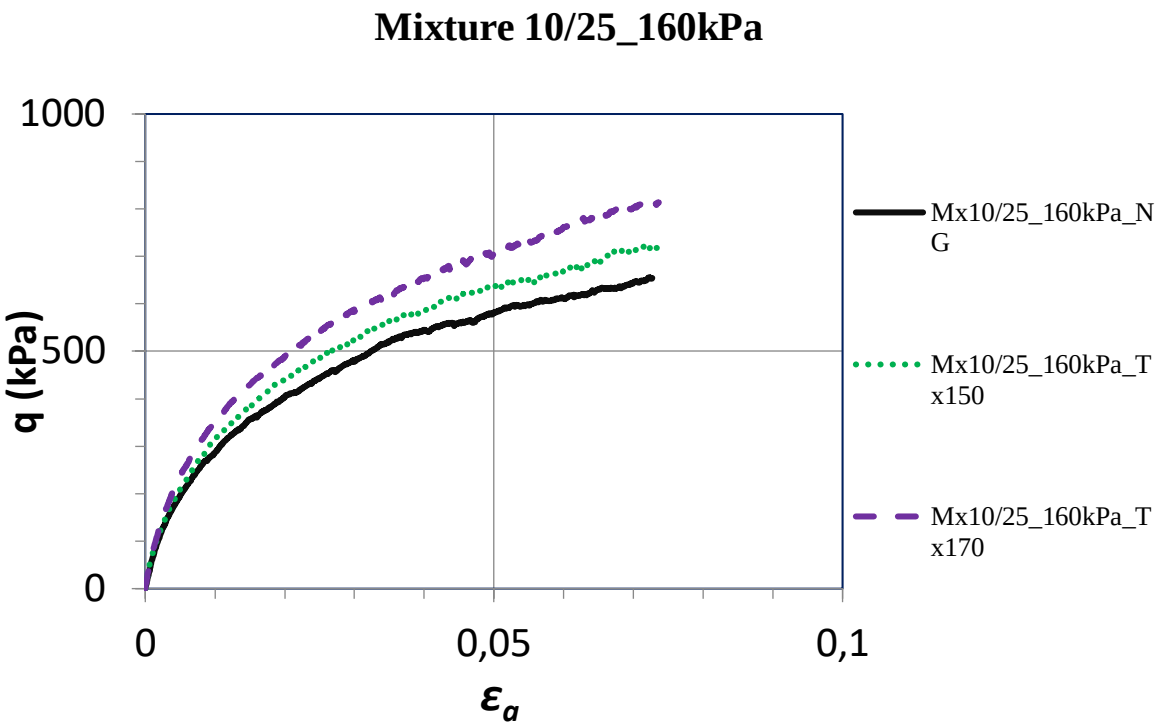

Figure 66. q v. ε_a plot for Mixture 10/25_160kPa.

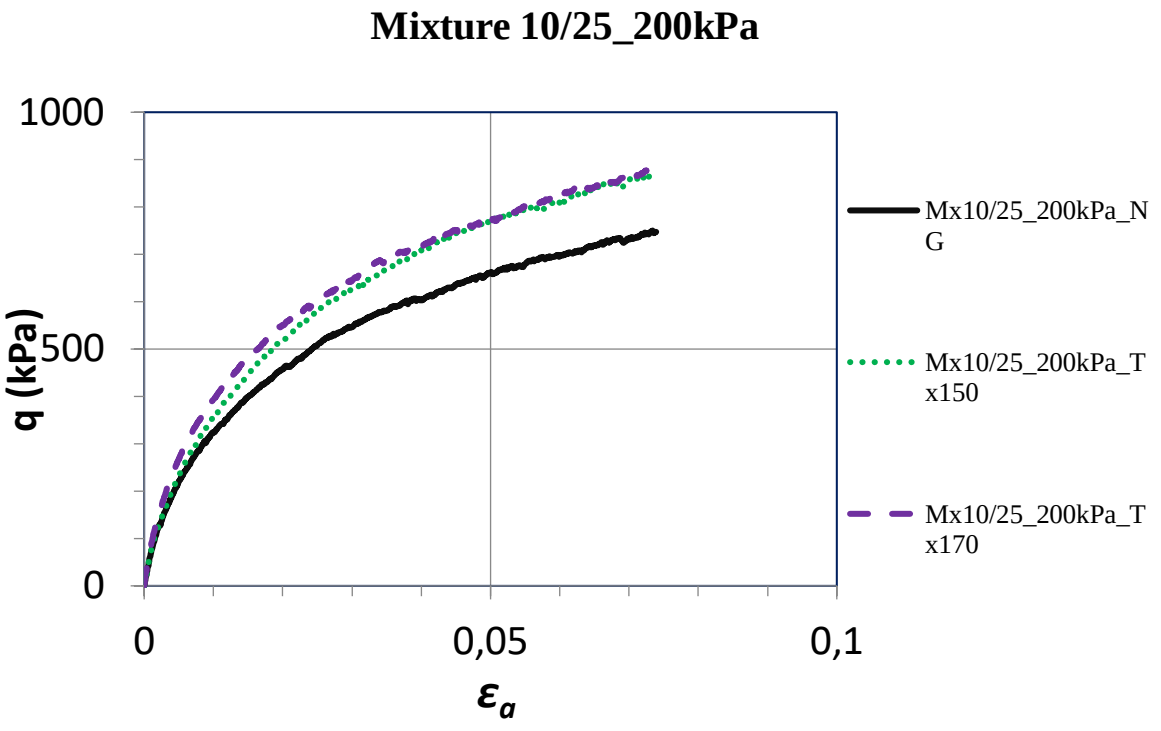

Figure 67. q v. ε_a plot for Mixture 10/25_200kPa.

Mixture 10/25 was sieved after each performed test and the plot of percentage of the gravels finer than 10 mm against confining stress was built. It can be stated that with the increasing reinforcement conditions amount of the material removed after each test has decreased. Thereby, proving

that partially interlocking of the aggregates results in an increase of lateral resistant and decrease of the friction between aggregates at geogrid level. However, for the reinforced gravel at high confining pressures the percentage of waste material was found to be approximately equal; thus, may be caused by the partially breakage of the geogrids as illustrated in Figure 69. Nevertheless, efficiency of the geogrid in diminishing soil abrasion during shear has been proved.

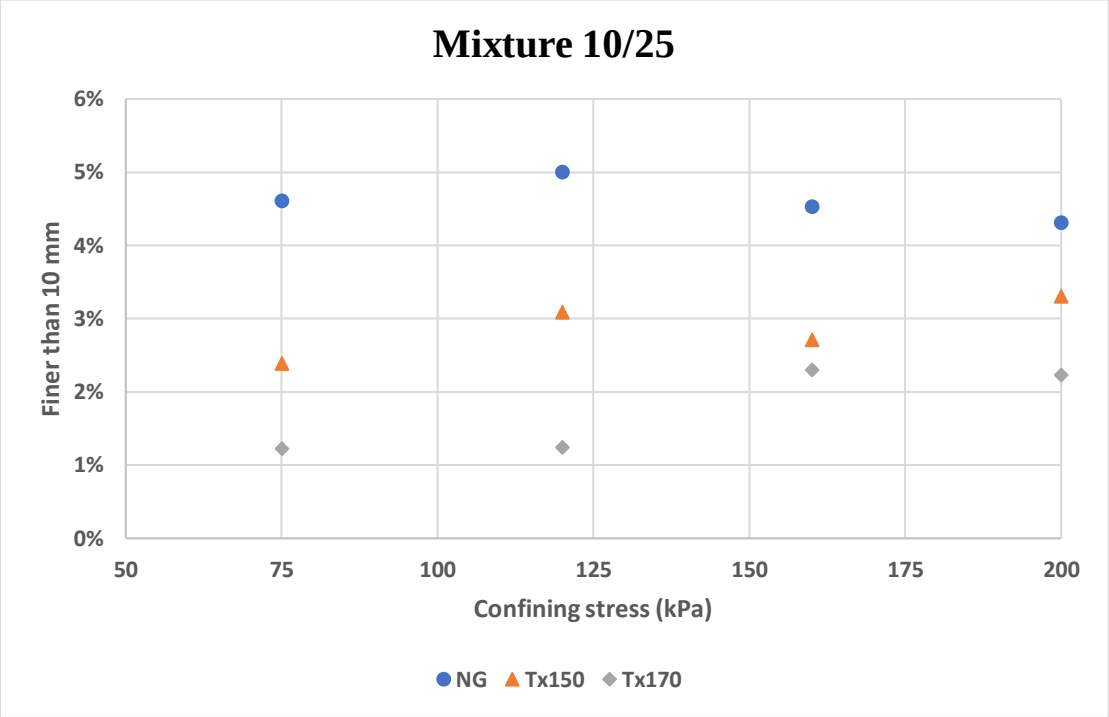

Figure 68. Material finer than 10 mm sieve.

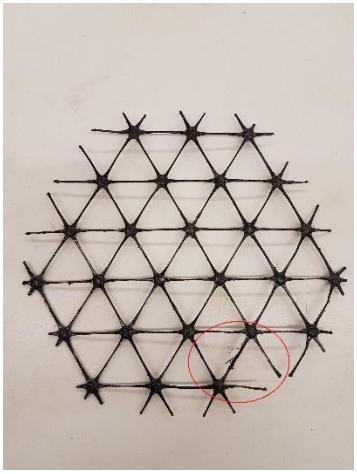

Figure 69. Partially broken geogrid after test Mx10/25_160kPa_Tx170.

8.3. Comparison of Mx0/25 and Mx10/25

Test results for different mixtures are discussed in this section. Peak strength (from Figure 70 to Figure 72) plots are presented for both mixtures at 7% of axial deformation. As it is seen strength of the Mixture 0/25 was found to be larger for reinforced and non-reinforced cases.

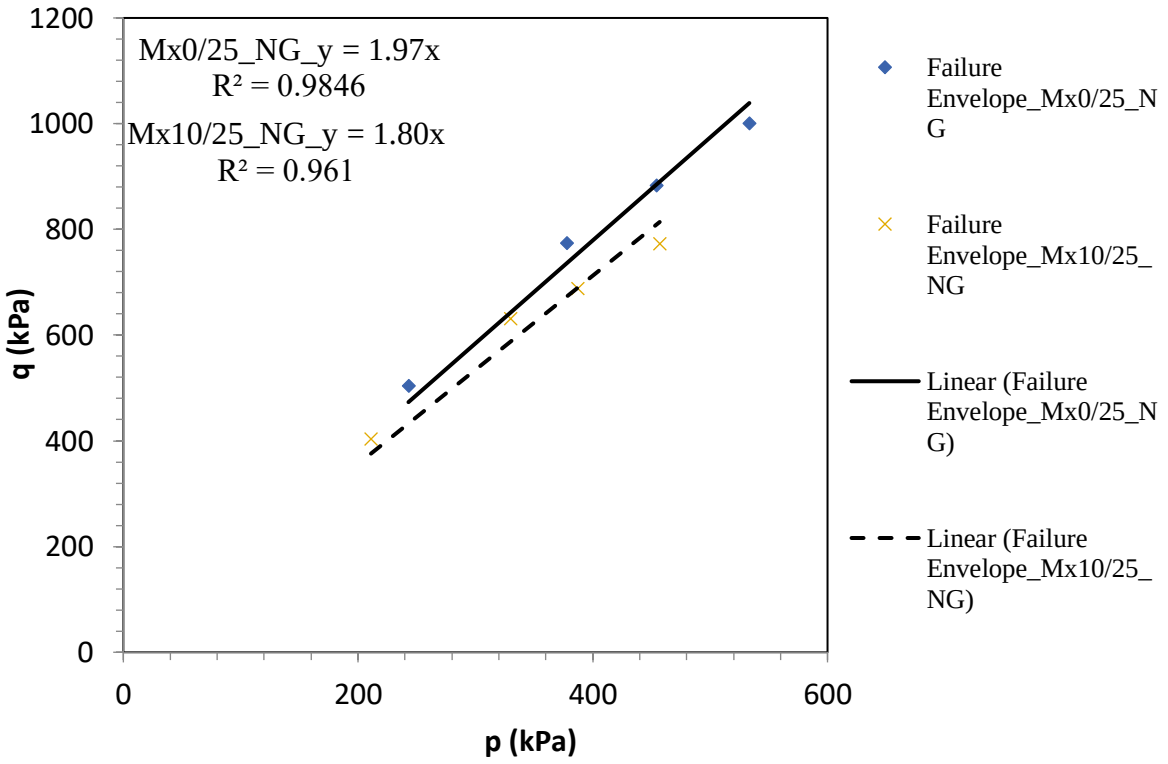

Figure 70. Peak strength for Mixture 0/25 and 10/25 without geogrid.

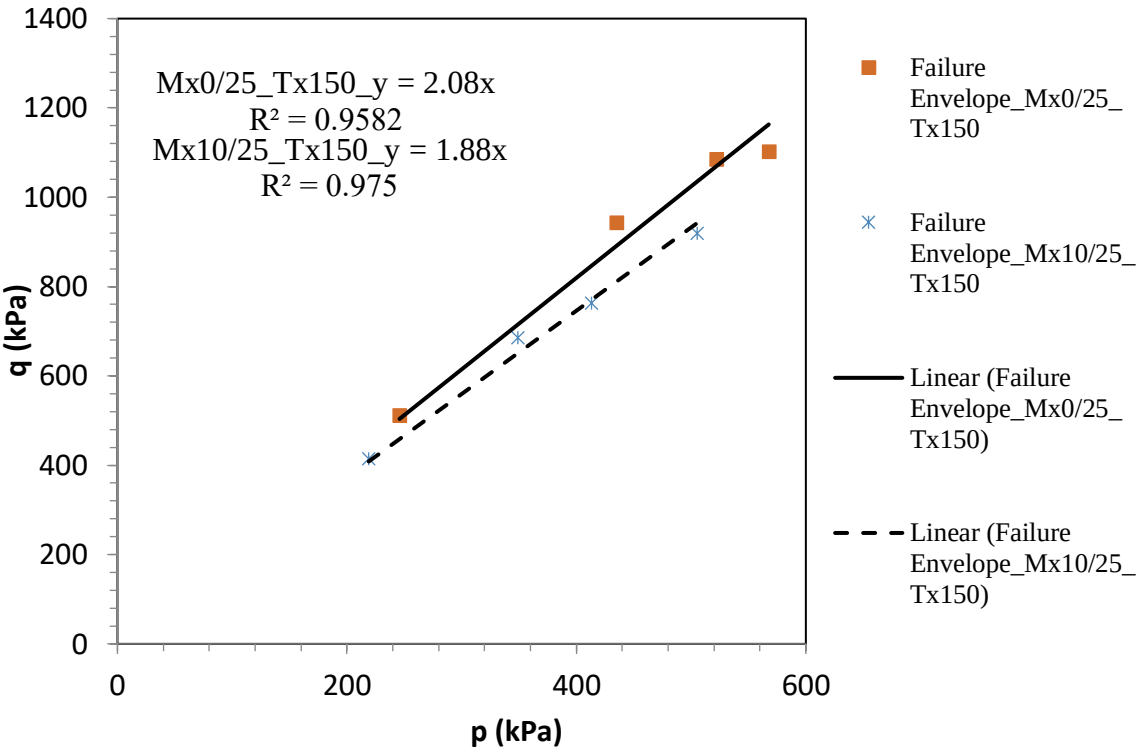

Figure 71. Peak strength for Mixture 0/25 and 10/25 with geogrid Tx150.

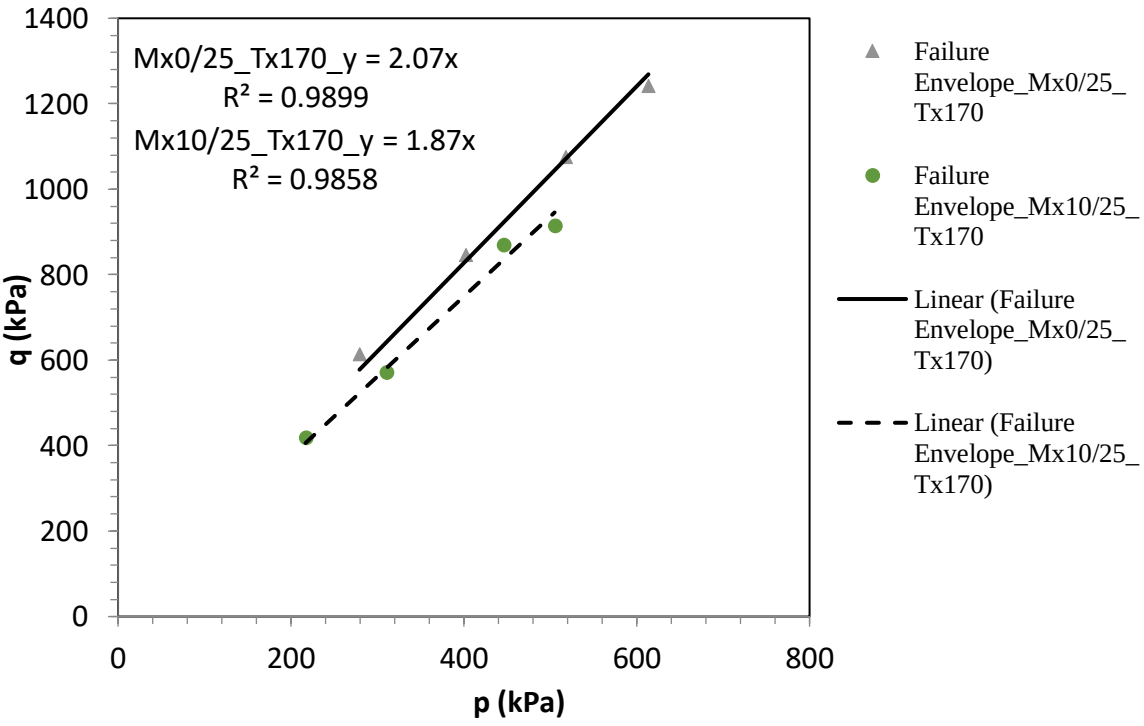

Figure 72. Peak strength for Mixture 0/25 and 10/25 with geogrid Tx170.

Changing grain size distribution results in a friction angle to reduce, as summarized in Table 8. Collins et al. (1992) suggested following relationship for the peak friction angle (φ'_{peak}):

$$\varphi'_{\text{peak}} = \varphi'_{cs} + \text{A}\left(e^{-\xi_0} - 1\right) \geq \varphi'_{cs}$$

Where, A is a soil type parameter, ξ_0 is an initial state parameter which is defined as a difference of initial void ratio and the void ratio at critical state line, and φ'_{cs} is a critical-state friction angel, which is independent of GSD (Li a t., 2014). Decrease of the peak frictional angle is related to the grain crushing that creates a contractive volumetric behavior. Furthermore, as the coefficient of uniformity increases critical-state line (CSL) moves downward on *e - p'* plane as illustrated in Figure 73. Thereby, uniformly graded material tends to dilate less in order to reach the CSL's than the well graded aggregates. As a result, void ratio at CSL for well graded soil will be larger leading to a greater value of friction angle (Li a t., 2014).

Finally, the effect of geogrid reinforcement may be expressed as a factor of safety (FS) computed as a function of frictions angles. This FS was calculated by following equation:

$$FS = \frac{\tan(\varphi'_1)}{\tan(\varphi'_0)}$$

Where, φ'_1 is a friction angle for mixture reinforced by geogrid and φ'_0 is a friction angle of non-reinforced sample. Table 9 represents obtained safety factors for Mx0/25 and Mx20/25, as it can be seen that geogrid improvement was relatively more efficient in the well graded material.

Table 8. Summarized strength envelope parameters for Mx0/25 and Mx10/25.

Pa-ram eter	Mx0/25_N G	Mx10/25_ NG	Mx0/25_Tx1 50	Mx10/25_Tx1 50	Mx0/25_Tx1 70	Mx025_Tx1 70
M	1.97	1.80	2.08	1.88	2.08	1.87
φ'	47.8°	43.5°	50.5°	45.3°	50.5°	45.5°

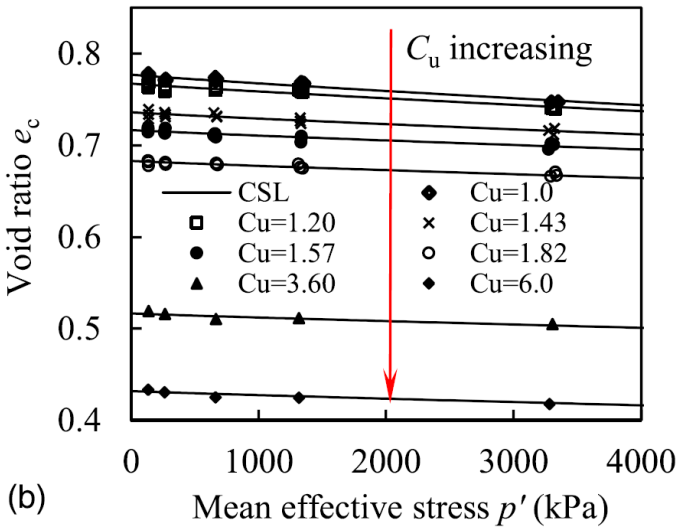

Figure 73. CSL in *e-p'* plane.

Table 9. Factor of safety of geogrids.

	Mx0/25	Mx10/25
Tx150	1.10	1.07
Tx170	1.10	1.08

9. Summary and conclusions

The application of geogrids and available techniques that can be applied for evaluation of soil-geogrid interactions are discussed in literature review. Among these methods, confined laboratory testing was selected for this research. Furthermore, a newly commissioned large triaxial cell was use for testing. Material part included information about different types of soil and geogrid. Testing procedure, starting with the membrane moulding and finishing by the placement of triaxial cell under frame load were reported. Experimental results were analysed in terms of different mixtures, types of geogrid, and confining pressure.

Main results obtained can be summarized as follows:

- The newly commissioned large triaxial cell at the geotechnical lab in UPC has been proven useful to study geogrid reinforced soils
- A very light compaction procedure capable of obtaining good repetitivity in initial state has been devised
- Testing of geogrid reinforces gravels requires special procedural precautions to avoid puncturing the membranes or damaging the instrumentation

- For the same compaction procedure, the well graded mixture attained higher initial densities than the uniform gravel
- Early contraction followed by dilatant behaviour were observed for all mixtures, expect anomalous instances where membrane breakage occurred.
- Geogrids improved the peak frictional angle for both the uniform and the well graded mixture.
- Geogrids were also shown efficient in diminishing granular material attrition during shearing
- Comparison of the two mixtures showed that geogrid reinforcement, expressed as sextra safety factor on friction, was relatively more beneficial for the well graded soil.

Future works are suggested by the results of this research, particularly with respect to the future use of the new equipment. For instance, testing with an increased number of LVDT's seems necessary to better observation of the dilatancy effect. Also, scratch on the piston should be eliminated, to increase maximum axial deformation available for all specimens and allow the test to continue up to critical state.

Reference

Alvarado de Menéndez, C. E. Hydro-mechanical behavior of coarse aggregates. *PhD Thesis, UPC, Department of Civil and Environmental Engineering*, 2017.

Chen, X., Zhang, J., & Li, Z. (2014). Shear behaviour of a geogrid-reinforced coarse-grained soil based on large-scale triaxial tests. Geotextiles and Geomembranes, 42(4), 312-328.

Collins, I. F., Pender, M. J., and Yan, W. "Cavity expansion in sands under drained loading conditions." *Int. J. Numer. Anal. Meth. Geomech.*, 16: 3–23, 1992.

Giroud, J. P., & Han, J. Design method for geogrid-reinforced unpaved roads. I. Development of Design Method. *Journal of Geotechnical and Geoenvironmental Engineering*, *130*(8), 787-797, 2004.

Giroud, J. P., & Noiray, L. Geotextile-reinforced unpaved road design. *Journal of Geotechnical and Geoenvironmental Engineering*, *107*(ASCE 16489), 1981.

Haas, R., Walls, J., & Carroll, R. G. *Geogrid reinforcement of granular bases in flexible pavements* (No. 1188), 1988.

Indraratna, B., Salim, W., & Rujikiatkamjorn, C. *Advanced rail geotechnology–ballasted track*. CRC press, 2011

Koerner, R. M. Designing with geosynthetics (fifth edition). Xlibris Corporation, 2005.

Kovačević, Meho Saša, Danijela Jurić-Kaćunić, Lovorka Librić, and Gordana Ivoš. "Engineering soil classification according to EN ISO 14688-2: 2018." *Građevinar* 70, no. 10, 873-879, 2018.

Lade, P. V. Triaxial testing of soil (first edition). John Wiley & Sons, Ltd, 263, 277, 2016.

Lees, A. (2017). Simulation of geogrid stabilization by finite element analysis. In Proceedings of 19th International Conference on Soil Mechanics and Geotechnical Engineering, Seoul (pp. 1377-1380).

Li, Gang, Ying-Jing Liu, Christophe Dano, and Pierre-Yves Hicher. "Grading-dependent behavior of granular materials: from discrete to continuous modeling." *Journal of Engineering Mechanics* 141, no. 6 (2014): 04014172.

Mehrjardi, G. T., Ghanbari, A., & Mehdizadeh, H. Experimental study on the behaviour of geogrid-reinforced slopes with respect to aggregate size. *Geotextiles and Geomembranes*, 44(6), 862-871, 2016.

Patra, C., N. Sivakugan, and B. Das. "Relative density and median grain-size correlation from laboratory compaction tests on granular soil." *International journal of geotechnical engineering* 4, no. 1, 55-62, 2010.

Youd, T. L. "Factors controlling maximum and minimum densities of sands." In *Evaluation of relative density and its role in geotechnical projects involving cohesionless soils*. ASTM International, 1973.

Zornberg, J. G., & Gupta, R. Geosynthetics in pavements: North American contributions. In Theme Speaker Lecture, *Proceedings of the 9th International Conference on Geosynthetics, Guarujá, Brazil,* May (Vol. 1, pp. 379-400), 2010.